Groundwater processes in Saharan Africa: Implications for landscape evolution in arid environments

Abotalib Z. Abotalib, Mohamed Sultan, Racha Elkadiri

PII: S0012-8252(16)30049-6
DOI: doi: 10.1016/j.earscirev.2016.03.004
Reference: EARTH 2237

To appear in: *Earth Science Reviews*

Received date: 18 September 2015
Revised date: 3 February 2016
Accepted date: 11 March 2016

Please cite this article as: Abotalib, Abotalib Z., Sultan, Mohamed, Elkadiri, Racha, Groundwater processes in Saharan Africa: Implications for landscape evolution in arid environments, *Earth Science Reviews* (2016), doi: 10.1016/j.earscirev.2016.03.004

Table 1

Groundwater processes in Saharan Africa: Implications for landscape evolution in arid environments

Abotalib Z. Abotalib,[a, b] Mohamed Sultan,[a] Racha Elkadiri[a,c]

(*a) Department of Geosciences, Western Michigan University, 1903 West Michigan Avenue, Kalamazoo, Michigan 4900 8, USA.*

(b) Department of Geology, National Authority for Remote Sensing and Space Sciences, Cairo 1564, Egypt.

(c) Department of Geosciences, Middle Tennessee State University, Murfreesboro, Tennessee 37132, USA.

Corresponding Author: Mohamed Sultan, Department of Geosciences, Western Michigan University, 1903 West Michigan Avenue, Kalamazoo, Michigan 49008, USA.

Office and voice mail: 269-387-5487; Lab: 269-387-545; Fax: 269-387-5513; E-mail: mohamed.sultan@wmich.edu

Table 1

ABSTRACT

Paleoclimatic regimes over Saharan Africa alternated between dry and wet periods throughout the Pleistocene Epoch, and it is during the wet periods that the Saharan fossil aquifers were recharged. We investigated the role of groundwater-related processes in shaping the Saharan landforms (e.g., theater-headed valleys [THV]; depressions, escarpments, playas, and tufa deposits) over areas occupied by the largest of these aquifer systems, the Nubian Sandstone Aquifer System (NSAS; area: 2.6 million km^2) in Egypt, Libya, Sudan, and Chad. We reviewed the suggested hypotheses for the origin of these landforms in the Sahara and in similar settings elsewhere and present evidence (remote sensing-based landscape analysis, geostatistical and geospatial analyses, hydrological, lithological, isotopic and field) in support of the following: in Pleistocene wet periods groundwater under high hydrostatic pressures accessed deep-seated structures, discharged at the free faces, THV developed, scarps retreated, fluvial (in wet periods) and aeolian processes (in dry periods) together with seepage weathering eroded and transported loose debris, and depressions were formed. Evidence includes: (1) extensive distribution of THV (stubby-looking geometry, theater-like heads, U-shaped profile, flat floors, and structurally controlled patterns) indicative of sapping processes were mapped (using a GIS-based logistic regression model) along faulted scarps extending for over 1450 km in the NSAS; (2) widespread distribution of tufa deposits plastered on scarp faces of the natural depressions within the NSAS with isotopic compositions consistent with deposition from NSAS fossil groundwater (δ^{18}O: −12.8 to −8.0‰); (3) absence of well-developed drainage systems over the Libyan Plateau; (4) onset of endorheic streams from the identified THV along the NSAS escarpments (within the Qattara, Kharga, Farafra, and Dakhla depressions) and at the boundary between massive limestone formations (e.g., Gara, Kurkur, and Marmarica) and underlying erodible shale and

Table 1

argillaceous sandstone formations (e.g., Dakhla and Moghra) consistent with a groundwater discharge origin for the endorheic streams; (5) reported carbonate-rich playa deposits within scarp-foot depressions at the terminations of the endorheic streams; (6) artesian upward leakage of depleted NSAS groundwater (δD: −81 to −72‰; and $\delta^{18}O$: −12.8 to −8.0‰) into shallower Oligocene, Miocene, and Pliocene aquifers (δD: −0.7 to 7.2‰; $\delta^{18}O$: −1.13 to 1.20‰) as evidenced by the mixed isotopic composition (δD range: −62.6 to −2.6‰; $\delta^{18}O$ range: −7.0 to −1.09‰) of groundwater. Understanding the role of groundwater processes in landscape evolution over areas occupied by the NSAS has implications for understanding the development of landscape in Saharan Africa, Arabian Sahara, similar settings worldwide, and the evolution of the Martian landscape.

KEYWORDS:

Arid zone geomorphologic processes, remote sensing, theater-headed valleys, groundwater sapping, Egypt, Nubian Sandstone Aquifer System

Table 1

1. INTRODUCTION

The Saharan Desert is the largest hyper-arid area (9,400,000 km^2) on Earth, receiving less than 5 mm of average annual precipitation (New et al., 2000). It extends from the Atlantic Ocean in the west to the Red Sea Hills in the east, and from the Mediterranean Sea in the north to the Sahel zone in the south. Previous studies on the distribution and origin of fossil groundwater, fluvial landforms, and paleo-channel river systems, wind regimes, and deposits (e.g., tufa, playas, and cave fillings) indicate that paleoclimatic regimes of the North African Sahara alternated between dry and wet periods throughout the past several million years (Szabo et al., 1995; Smith et al., 2004a, 2004b; Sultan et al., 2007; Abouelmagd et al., 2012). During the wet periods the aquifers in North Africa were recharged during interglacial periods through the intensification of the paleo-monsoons (Yan and Petit-Maire, 1994) or in glacial periods by intensified paleo-westerlies (Sultan et al., 1997, Sturchio et al., 2004; Abouelmagd et al., 2012); during these periods a considerable rise of the paleo-piezometric surfaces was reported (Causse et al., 1989; Pachur and Hoelzmann, 2000). The largest of these aquifer systems is the Nubian Sandstone Aquifer System (NSAS; area: 2.6×10^6 km^2) in Egypt, Libya, Sudan, and Chad. The NSAS occupies around 20% of the Sahara (Fig. 1). There are other large fossil aquifers such as the North Western Sahara Aquifer System (NWSAS; area: 1.2 million km^2) in Algeria, Tunisia, and Libya, and smaller fossil aquifers ($<900 \times 10^3$ km^2) including the Iullemeden Aquifer, the Western Sahara Aquifer, and the Taoudeni Aquifer (IGRAC, 2012; Fig. 1). Similar fossil aquifers (e.g., the Upper Mega Aquifer) were reported from the neighboring deserts in Arabia.

Areas occupied by the NSAS are dominated by extensive outcrops of flat-topped carbonate plateaus, hereafter referred to as the Libyan Plateau, and natural depressions (Kharga, Dakhla, Farafra, Bahariya, and Qattara depressions; Fig. 1) that cover large areas and are bound

Table 1

by escarpments. Deep canyons, hereafter referred to as theater-headed valleys (THV), are incised in these escarpments and playas and tufa deposits are found proximal to these escarpments. The origin of these escarpments, natural depressions, THV, tufa and playa deposits and the role of groundwater as a denudational process in shaping the landscape has not been fully investigated. In this manuscript, we review and further investigate the proposed models for the origin of depressions and THV and provide additional evidences in support of a major role for groundwater processes in the development of THV, depressions, escarpments, and groundwater-related deposits (e.g., tufa and playas).

Proposed origins for the natural depressions and bounding escarpments include wind deflation, fluvial systems and stream erosion, tectonic deformation, and salt weathering. The presence of cliffs in the upwind side of the Qattara, Siwa, Farafra and Dakhla depressions, the gentle slopes in the downwind side (Aref et al., 2002) and the abundance of dune fields along the wind trajectory downwind of the depressions supports the wind deflation hypothesis (Ball, 1927; Squyres and Bradley, 1964). However, wind deflation alone cannot breach the limestone cap rocks, a condition that is required to expose the underlying clastic strata to erosion and deflation by aeolian processes (Albritton et al., 1990). Fluvial systems and stream erosion models (McCauley et al., 1982; Said, 1983; Albritton et al., 1990) provide adequate solutions for the removal of the limestone cap rock by integrated surficial erosion, karstic and mass wasting processes, yet the absence of notable exorheic streams (Kropelin, 1993) that drain toward depressions sheds doubt on the validity of this model. A tectonic origin for the Dakhla and Kharga oases is supported by the thin sedimentary cover (~120 m) and the structural expression of the basement uplifts in these areas (Said, 1979; Gindy, 1991), but is less relevant for the depressions within the northern Libyan Plateau, an area that is identified as being a stable shelf

Table 1

since the Early Miocene (Albritton et al., 1990; Abdeldayem, 1996). Erosion by salt weathering coupled with wind and stream activity (Aref et al., 2002) is supported by the extensive distribution of salt weathering-related features in Eastern Sahara (Goudi, 2013), but the model cannot account for the presence of deep canyons within the escarpments and for the associated mass wasting.

The role of groundwater as a denudation process that locally shaped the landscape of the Sahara was suggested by Maxwell, (1982); he stated that the deep erosional canyons incised into the Gilf Kebir Plateau was accomplished by cliff sapping and spring discharge, but the mechanism of erosion remained ambiguous until the groundwater sapping processes were explained and modeled by Luo et al (1997). Specifically, they modeled groundwater discharge along deep-seated faults bounding the escarpments of the Kharga depression in the Western Desert of Egypt, mass transport by discharged water, escarpment retreat, and development of THV along the compromised escarpments.

The term "groundwater sapping" refers to the undermining, collapse, and retreat of valley head and side walls by the weakening or removal of the basal support as a result of weathering and erosion processes associated with the groundwater outflow along the seepage plane (Dunne, 1980; Laity and Malin, 1985; Irwin et al., 2014). Stream networks associated with groundwater sapping processes differ from those related to overland flow stream systems in their overall patterns, stream characteristics (stream profile, width, density, and onset location), and the degree to which structures control stream distribution (Laity and Malin, 1985; Luo et al., 1997; Hoke et al., 2004).

For several decades, THV have been considered by default as groundwater sapping–related landforms in many areas worldwide, including the Western Desert, Egypt (Luo et al.,

Table 1

1997); Hackness Hills, England (Nash, 1996); Apulia region, southern Italy (Mastronuzzi and Sanso, 2002); Altiplano plateau, northern Chile (Hoke et al., 2004); slopes of the Kohala volcano, Hawaii, USA (Kochel and Piper, 1986); the Colorado Plateau, USA (Laity and Malin, 1985); the Southern High Plains, USA (Wood, 2002); Obara Hills, Japan (Onda, 1994); and the Canterbury Plain, New Zealand (Schumm and Phillips, 1986). The THV were also recognized on the Martian surface (Higgins, 1982; Kochel and Piper, 1986; Malin and Edgett, 2000).

The proposed groundwater origin for the formation of THV was later challenged by findings from field and experimental studies. These studies indicated that the valleys should not be exclusively attributed to groundwater seepage, but other processes (e.g., megaflooding, waterfall erosion, landslides, and differential weathering) could play a major role in their formation as well (Lamb et al., 2006, 2008, 2014; Lamb and Dietrich, 2009; Craddock et al., 2012; Marra et al., 2014; Irwin et al., 2014). The major arguments that were advanced against the seepage erosion origin is the bedrock strength and the large size of THV, which requires not only extensive weathering and/or the presence of gigantic water discharge to disintegrate bedrock and remove (transport) weathering products away from the escarpment, but also for these processes to be active for substantial timespans to remove the large amounts of weathered material (Howard and Kochel 1988; Howard and Selby, 1994; Lamb et al., 2006).

In this manuscript, we show that the aforementioned conditions for groundwater processes including sapping activity prevailed during the previous wet Pleistocene periods in the Sahara and played a major role in modifying the Saharan landscape. We advocate that during the wet climatic periods pressurized groundwater accessed deep-seated faults, caused prolonged and extensive discharge, incised THV, undermined escarpments and caused them to retreat, left tufa plastered on escarpment faces and playa deposits proximal to these cliffs, and depressions were

Table 1

formed. Our approach calls on the application of statistical models and integration of observations from remotely acquired data, field observations, geological, geomorphological, and isotopic data to accomplish the following: (1) delineate THV across the NSAS; (2) investigate the distribution of THV, playas, and tufa deposits in relation to that of the escarpments and stream networks in search of causal effects in the Qattara, Kharga, Farafra, and Dakhla depressions; (3) examine the origin of the tufa and playa deposits, and (4) test the assumption of artesian upward leakage from deep to overlying shallow aquifers by examining the isotopic composition of groundwater samples. We will also show that addressing the role of groundwater processes in shaping the Saharan landscape will not only improve our understanding of the evolution of the Sahara, but will shed light on the evolution of similar terrestrial (Arabia) and extraterrestrial analogs (Mars).

2. GEOLOGIC, HYDROLOGIC, AND TOPOGRAPHIC SETTINGS OF THE NSAS

The NSAS is largely composed of: (1) pre–Upper Cretaceous continental sandstone formations (Nubian Aquifer System [NAS]), and (2) Upper Cretaceous–Tertiary marine carbonates that give way to Mio-Pliocene sandy formations (Post-Nubian Aquifer System [PNAS]) and build up the so-called Libyan Plateau (Fig. 2) (Thorweihe, 1990; Bakhbakhi, 2006). The continental and marine sequences in the NSAS are separated by confining shale and clay layers of Cenomanian age (Thorweihe and Heinl 2002). The thickness of the marine carbonates overlying the NAS aquifer increases northward (from 400 to 2000 m; Shata, 1982).

The NSAS is heavily dissected by sub-vertical deep-seated faults, many of which are basement structure that were reactivated by tectonic activities at later time periods (Neev et al.,

Table 1

1982; Sultan et al., 2007). These include east-west—trending (Kalabsha trend) and northeast-southwest—trending (Pelusium trend) fault systems in the southern and northern Western Desert, respectively (Neev et al., 1982; Hermina, 1990; Thurmond et al., 2004; Khan et al., 2014).

Measurements of radiochlorine (^{36}Cl) and radiokrypton (^{81}Kr) isotopes in deep groundwater from the northern regions of the NSAS indicate very long residence time (up to 1.3×10^6 years; Sturchio et al., 2004; Patterson et al., 2005) except for areas proximal to the recharge areas, where reported ages do not exceed a few tens of thousands of years (Haynes and Haas, 1980). The recharge areas for the NSAS are found in the south, where the NAS crops out. Unconfined aquifer conditions prevail in the south and give way to confined conditions north of latitudes 25°N (Sturchio et al., 2004), giving rise to a regional groundwater flow from southwest to northeast and from south to north (Shata, 1982; Thorweihe, 1990; Salem and Pallas, 2004).

Because of the extensive faulting in the NAS (Neev and Hall, 1982; Shata, 1982; Thorweihe, 1990) and the high artesian pressure of the overlying thicknesses, artesian upward leakage takes place along deep-seated faults and recharges the overlying PNAS aquifer (Shata, 1982; Sultan et al., 2007). Furthermore, discharge occurs in depressions where the groundwater level intersects the surface. These depressions enclosed several paleolakes during Pleistocene wet periods and are now the sites of playa deposits under present dry conditions. Examples include the Balat and Bahr playas in Egypt (Hassan et al., 2001; Brookes, 2010) (Fig. 1). Under present-day arid conditions, discharge in closed depressions (e.g., the Qattara depression in Egypt) produces evaporative sabkha deposits (Aref et al., 2002; Salem and Pallas, 2004).

As described earlier, the landscape of the NSAS is dominated by extensive flat-topped, gently dipping strata that are truncated by depressions and escarpments, many of which are structurally controlled (Said, 1979; Robinson, 2002). Proximal to, and at the foothills of, these

Table 1

escarpments are springs and depressions; plastered on the walls of some of these escarpments, and located at scarp-foot depressions (e.g., the Kharga and Dakhla depressions) (Fig. 3), are groundwater tufa deposits of varying ages (Smith et al., 2004a; Adelsberger and Smith, 2010; Brookes, 2010). For example, tufa ages ranged from 50 to 600 ka in the Kharga depression, and from 80 to 620 ka in the Dakhla depression (Smith et al., 2004a; Brookes, 2010; Jimenez, 2014). The THV were reported in the Kharga and Farafra depressions and the following features were identified as indicative of their presence: (1) headward channel growth; (2) scallop-shaped escarpment edges; (3) stubby-looking geometry; (4) theater-like heads; (5) a U-shaped profile with valley-width ratio exceeding 1.0 (Pedrera et al., 2009); (6) flat floors; and (7) structurally controlled patterns (Luo et al., 1997). These features, together with three additional features (1) low stream order; (2) asymmetrical drainage patterns (Laity and Malin, 1985; Kochel and Piper, 1986; Schumm et al., 1995); and (3) high junction angles (>55˚; Kochel and Piper, 1986; Devauchelle et al., 2012) were used to delineate similar THV in the Colorado Plateau, Hawaii, and Florida Panhandle.

A wide distribution of features indicative of the presence of THV was revealed from the examination of Google Earth images draped over digital topography and cross sections across valleys in the Kharga and Farafra depressions, the areas where Lou et al., (1997) first reported their presence, and in the Qattara depression (Fig. 4).

3. DATA SETS

We adopted an integrated approach that utilizes statistical modelling as well as a spatial analysis of field, remote sensing, isotopic, and chronologic datasets in a geographical information system (GIS) to investigate the role of groundwater discharge in the evolution of the

Table 1

Saharan landscape. The collection and analysis of data was carried out on both the local and regional scales. We co-registered all datasets to a unified projection (Datum: WGS-84; UTM Zone: NSAS N36, NWSAS N32, Upper-Mega Aquifer System N38) in a GIS environment.

3.1 Remote sensing data sets

Remote sensing data sources include: (1) Advanced Spaceborne Thermal Emission and Reflection Radiometer (ASTER) digital elevation model (DEM) mosaics (scenes: 12; spatial resolution: 30 m; source: USGS website[1]; coverage: the Qattara, Kharga, Farafra and Dakhla depressions in Egypt, Gebel El-Gharbi in the NWSAS, and Al-Guwifa area in Saudi Arabia), Shuttle Radar Topography Mission (SRTM) DEM mosaics (tiles: 475; spatial resolution: 90 m; source: USGS website; coverage: NSAS, NWSAS, and Najd Plateau); (2) painted hillshade images for the NSAS, the NWSAS, and Najd Plateau derived from the DEMs using the Arc hillshade tool (ESRI Arc GIS v.10); (3) drainage networks and watershed boundaries extracted from SRTM and ASTER DEMs using D8 flow direction algorithms (O'Callaghan and Mark, 1984) in Arc Hydro tool (ESRI Arc GIS v.10); (4) Landsat 4-5 Thematic Mapper (TM) mosaic bands 7, 4, and 2 (scenes: 11; spatial resolution: 30 m; source: Global Land Cover Facility database[2]; coverage: north Western Desert of Egypt); (5) false-color composite (blue: band 2; green: band 4; and red: band 7) Landsat 8 mosaic (three scenes; spatial resolution: 30 m source: USGS website; coverage: the Kharga depression in Egypt, Gebel El-Gharbi in the NWSAS, and Al-Guwifa area in Saudi Arabia); (5) high-resolution 3D models generated from Landsat 8 and ASTER DEM following the application of a resolution merge (Gram-Schmidt Pan Sharpening method; Li et al., 2004) of multispectral Landsat 8 images (30 m resolution) with panchromatic

[1] http://earthexplorer.usgs.gov
[2] www.landcover.org

Table 1

Landsat 8 images (15 m resolution); (6) Radarsat-1 mosaic (tiles: 2; spatial resolution: 30 m; source: Canadian Space Agency website[3]; coverage: Egypt and northern Sudan); (7) Geoeye images (scenes: 8; spatial resolution: 1 m; source: Google Earth imagery; coverage: Qattara, Kharga, and Farafra depressions; (8) merged Advanced Land Imager (ALI) (scenes: 1; spatial resolution: 10 m; source: USGS website; coverage: Qattara), and (9) Mars datasets including Mars Orbiter Laser Altimeter (MOLA) mosaic and the High-Resolution Stereo Camera (HRSC) mosaic (ESA/DLR/FU Berlin; source: the Geosciences Node of NASA's Planetary Data System at Washington University in St. Louis).

3.2 Geologic maps

We utilized the following geologic maps: (1) mosaicked geologic map for the Western Desert (scale: 1: 500,000; sheets: 15; coverage: Western Desert, Egypt; Klitzsch et al., 1987); (2) mosaicked geologic map for the northern Western Desert (scale: 1: 250,000; sheets: 25; coverage: north Western Desert, Egypt; El-Hinnawi et al., 2006); (3) mosaicked geologic map for the south Western Desert (scale: 1: 250,000; sheets: 30; coverage: south Western Desert, Egypt ; El-Hinnawi et al., 2005); (4) distribution of deep-seated and surface regional faults for the Western Desert (coverage: Western Desert, Egypt; Klitzsch et al., 1987; El-Hinnawi et al., 2005; 2006; Wescot et al., 2011); (5) detailed stratigraphic sections for the Western Desert, Egypt (coverage: the Kharga, Farafra and Dakhla depressions; Hermina, 1990); and (6) distribution of tufa and playa deposits in the Western Desert (coverage: south Western Desert, Egypt; source: Crombie et al., 1997; Sultan et al., 1997; Smith, 2001; El-Hinnawi et al., 2005; Jimenez, 2014)

[3] http://www.asc-csa.gc.ca/eng/satellites/radarsat1/mosaic.asp

Table 1

3.3 Isotopic and chronological data

We collected twenty groundwater samples for isotopic analyses (H and O) from the Bahariya Oasis, tapping the Nubian Aquifer (10 samples), and from Wadi El-Natrun and Wadi El-Farigh areas (10 samples), tapping the Miocene and Pliocene aquifers (Table 1; Fig. 1). Wells were pumped for a minimum of 20 to 30 minutes prior to sample collection. Groundwater samples were collected in 100 ml polyethylene bottles and tightly capped. Stable isotope ratios of H and O in water were measured at ISOTECH Laboratories in Champaign, Illinois, USA using a Picarro cavity ring-down spectroscopy (CRDS) laser system (Lehmann et al., 2009). The isotopic data for samples are reported (Table 1) in terms of the conventional delta (δ) notation, in units of permil (‰) deviation relative to Vienna standard mean ocean water (V-SMOW; Coplen., 1996), whereby

$$\delta\ (‰) = [(R\ sample/R\ standard) - 1] \times 10^3 \quad (1)$$

and $R = {}^2H/{}^1H$ or ${}^{18}O/{}^{16}O$

For comparison purposes, we included additional reported analyses for samples from the northern part of the Western Desert from, (1) Oligocene, Miocene, and Quaternary aquifers in El-Fayum area (21 samples: Thompson, 2007), and from (2) Miocene, Pliocene, and Quaternary aquifers (30 samples: El-Gamal, 2005) (Fig. 1). Four groundwater samples (S.31, S.33, S.61, and S.62) were collected for ^{14}C dating along two east-west—trending traverses west of the Nile Delta. Dissolved inorganic carbon (DIC) was first extracted in a vacuum by acidifying the sample, and the extracted carbon dioxide was cryogenically purified from other reaction products

Table 1

and catalytically converted to graphite (Vogel et al., 1984). Graphite $^{14}C/^{13}C$ ratios were measured using the 0.5 MeV accelerator mass spectrometer at the University of Georgia Center for Applied Isotope Studies (Cherkinsky et al., 2010). The ^{14}C isotopic abundances are reported (Table 2) in percent modern carbon (pmC), relative to that in atmospheric CO_2 in 1950 (Stuiver and Polach, 1977). Model ages are given in radiocarbon years before 1950 (years B.P.), using a ^{14}C half-life of 5568 years. The error is quoted as one standard deviation and reflects both statistical and experimental errors. The data was corrected for isotopic fractionation. For comparison purposes, our results were compared to reported ^{14}C ages for groundwater samples collected along an east-west transect to the west of the Nile Delta (Aeschbach-Hertig et al., 2007).

4. METHODS AND FINDINGS

The adopted approach is a four-fold exercise. We first delineate the regional distribution of THV across the NSAS (Task I). We then investigate the spatial correlation between the delineated THV, playa and tufa deposits, stream networks, and distribution of stratigraphic units on a regional scale (Task II) and on a local scale in selected areas (Qattara, Kharga, Farafra, and Dakhla depressions) (Task III) in search of causal effects. Finally, we test the assumption of artesian upward leakage from deep to overlying shallow aquifers by examining the isotopic composition of groundwater samples in relation to the distribution of deep-seated faults (Task IV).

4.1 Delineation of the regional distribution of THV across the NSAS

Table 1

Visual inspection of image products similar to those shown in Fig. 4 indicated that THV are widespread across the NSAS. To enable mapping of these features over the NSAS and across the entire Sahara, we developed a GIS-based logistic regression (LR) model to predict the presence or absence of THV based on values of a set of predictor variables, all of which were extracted from remote sensing datasets. The application of the model encompassed four steps: database generation, model construction, model validation, and model output generation. We used the ten morphological characteristics listed above together with one additional feature (high valley height-width ratio [Vf]) (Fig. 4) to identify the locations of THV in the NSAS using remotely acquired data. The Vf was used to quantify the U-shaped cross section of THV (high Vf value: >1) relative to V-shaped valleys (Vf values: ~0) (Pedrera et al., 2009).

Because of the extensive area covered by the NSAS and the inaccessibility of large areas within the NSAS, the adopted methodology heavily relied on observations extracted from high-resolution satellite imagery (viewable in Google Earth) that were field-verified in selected locations (e.g., the Farafra and Qattara depressions in Egypt). Using these geomorphological criteria, we identified a total of 1500 THV-present points and 1534 THV-absent points. In the selection of the THV-present points, we targeted the onset of the valleys only. The THV in the NSAS range from tens of meters to few kilometers in cross section. Although the THV are larger in dimensions than gullies, both have similar morphological characteristics; the THV and gullies share the headward growth, theater- or amphitheater-like heads, paucity of stream tributaries, vertical sidewalls, and tendency to occur along steep slopes (Luo et al., 1997; Martinez-Casanovas et al., 2004; Hobbs et al., 2014;). To map the distribution of THV in the NSAS, we applied LR statistical methods and predictor variables that were successfully used to map large gullies and topsoil depressions related to groundwater sapping or runoff erosion in Spain, Italy

Table 1

and Turkey (Martinez-Casanovas et al., 2004; Fernandez et al., 2008; Akgun and Turk, 2011; Conoscenti et al., 2014). We used six predictor variables including: slope angle, plan curvature, profile curvature, drainage density, stream power index [SPI], and topographic wetness index [TWI]) images.

THV are characterized by steep slopes (Laity and Malin, 1985; Dune, 1990; Howard and Selby, 1994), negative plan curvatures (i.e., surface is increasingly concave towards valley sides), positive profile curvatures (i.e., surface is increasingly convex at higher elevations; Fernandez et al., 2008), low drainage density and low stream order (Laity and Malin, 1985; Kochel and Piper, 1986; Luo et al., 1997), and moderate SPI and TWI values given the high slope and small upslope contributing area for the THV. Our measurements for the 1500 THV-present points show that this is indeed the case (mean ± 1S: slope: 14.9° ± 6.5, plane curvature: −0.25±0.18, profile curvature: 0.17±0.06, stream density: 9.4±15.4, SPI: 8.6±1.2, TWI: 12.1±1.37).

We generated a lithologic binary (1,0) filter, a lithologic map with a spatial resolution of 90 m to identify areas with massive carbonate cap rock overlying easily eroded beds, a condition that was previously identified for the formation of THV in the Kharga depression (Luo et al., 1997). The model was applied only to the limestone-covered plateaus in Egypt and Libya; thus, the mapped THV are probably those that formed under conditions and settings similar to those identified in the Kharga area.

The LR-delineated distribution for the THV across the NSAS is an occurrence probability map ranging from 0 to 1. Fig. 3 shows the distribution of the THV at probabilities equal to, or exceeding, a threshold value of 0.9. Inspection of Fig. 3 and other data sets (e.g., DEM or slope image) indicate that the majority of the identified THV occur along the edges of the Libyan

Table 1

Plateau and along the escarpments of depressions within the plateau with a total length of 1450 km. Because we targeted the onset of these valleys in the selection of the THV-present points, the LR-delineated distribution includes the topmost locations of the THV (alcoves), whereas the main channels of the valleys were not incorporated (Fig. 5). The area occupied by the delineated alcoves was estimated at 3436 km^2. Additional description for the predictor variables, the Vf ratio, and model construction and validation is given in supplementary materials.

4.2 Spatial correlation between delineated THV, tufa and playa deposits, and stream networks

We correlated the spatial distribution of the delineated THV across the NSAS with that reported for tufa deposits (Sultan et al., 1997; Nicoll et al., 1999; Smith et al., 2004a, 2004b; Kieniewicz and Smith, 2009; Adelsberger and Smith, 2010; Torab, 2013; Jimenez, 2014) (Fig. 3). Inspection of Fig. 3 shows: (1) the delineated THV are concentrated along the peripheries of the Libyan Plateau escarpments and on the scarp faces of depressions within the Plateau, and (2) the reported occurrences and types (plateau, wadi, and basinal) of tufa deposits (Crombie et al., 1997; Smith et al., 2004b; Adelsberger and Smith, 2010; Brookes, 2010) and the majority of playa deposits (El-Hinnawi et al., 2005; El-Hinnawi et al., 2006) are proximal (<25 km) to the delineated THV (Figs. 3, 6, and 7). Scarp or plateau tufas are plastered along scarp faces at elevations exceeding present-day piezometric surfaces (i.e. 10–15 m below the level of the Libyan Plateau); compared to scarp tufa, wadi tufas are generally located at lower elevations and follow the old slope of the escarpment as thin inclined sheets or as thick horizontal strata (Smith et al., 2004b). Basinal tufas (also called spring tufa mounds) are associated with lacustrine playa

Table 1

deposits in scarp-foot depressions, with a maximum distance of 25 km from proximal escarpments (e.g., the Dakhla depression; Figs. 3 and 6).

We also correlated the spatial distribution of the delineated THV across the NSAS with the reported distribution of lacustrine playa deposits (El-Hinnawi et al., 2005, 2006) and the inferred distribution of the paleochannels (Fig. 7). We used two datasets to map the paleochannels: (1) radar imagery (C band from Radarsat-1) that penetrates (up to 50 cm) the dry fine-grained sand sheet in the study area and images the shallow subsurface features (Schaber et al., 1997), and (2) DEM from which the drainage network was extracted. A mosaic was generated from Radarsat-1 tiles over Egypt and Sudan. We extracted the major drainage networks from the DEM applying a high threshold value for the number of cells (50,000 cells) draining towards a downslope cell. The Radarsat-1 mosaic, the extracted drainage network, the delineated THV, and the reported playa deposits are all shown in Fig. 7. Inspection of radar imagery (Fig. 7), visible near-infrared (VNIR) imagery, our field observations, and those reported by Kropelin (1993) indicate that: (1) well-developed drainage systems are absent over the Libyan Plateau, and (2) locations of delineated THV mark the onset of drainage systems.

We observed a major west to east paleo-drainage pattern on the radar imagery (Fig. 7, dark interconnected channel networks) and in the DEM-derived channels (Fig. 7, blue lines). The source areas for this network are the Gilf Kebir Plateau and Uweinate highlands; one interpretation for the general correspondence between the radar paleochannels and the DEM-derived channels is that the sand sheet cover in these areas modulates, but does not obscure, paleotopography. Similar applications and findings were reported in the study area (Ghoneim and El-Baz, 2007).

Table 1

4.3 Landscape analysis of selected geomorphological sites in the NSAS

Additional insights into the origin of THV and natural depressions within the limestone Libyan Plateau and associated denudational landforms were gained from the landscape analysis of selected four geomorphological sites (Fig. 1) in the Qattara, Kharga, Farafra, and Dakhla depressions. The LR model results indicate abundant distribution of THV along escarpments in these locations. We compiled the published geological and structural datasets in a GIS environment, together with remote sensing data and field observations, to investigate the geologic and topographic characteristics of these locations. The studied sites display striking similarities in their geologic and topographic characteristics: (1) minimal contribution of the Libyan Plateau drainage systems (i.e. exorheic streams) into the depressions, (2) high structural control, (3) strong-over-weak stratigraphy, and (4) abundant denudational landforms and tracers for groundwater activity.

4.3.1 Minimal contribution of the Libyan Plateau exorheic drainage systems

We delineated drainage networks over the Libyan Plateau over areas where THV are prominent, extensive and deeply incised into the depressions-bounding escarpments in the four investigated regions (Qattara, Kharga, Farafra, and Dakhla). The networks were extracted from the DEM by applying a small threshold value for the number of cells (100 cells) draining towards a downslope cell. The extracted networks were then superimposed over the DEMs (Fig. 8). Inspection of Fig. 8 reveals the following in all investigated areas: (1) the surface of the Libyan Plateau gently slopes and drains away from the escarpment and, (2) we infer a minimal contribution of the surface runoff over the Libyan Plateau into the THV and their bounding escarpments given the limited extension of the catchment areas.

Table 1

We delineated the catchment area for a number of THV in each of the investigated regions. We first identified a snap pour point at a location that is approximately halfway along the valley's length (Fig. 8), and we then calculated the upstream contributing area using flow accumulation algorithms (Tarboton, 1997; Teng et al., 2008). We derived conservative estimates for the eroded volume of these valleys by first projecting the surface of the Libyan Plateau to its pre-incision location and then calculating the volume of rocks subtended between the projected surface and present-day DEM (Giaconia et al., 2012). The adopted methodology yields minimum estimates for the eroded rocks (Bellin et al., 2014). Our findings reveal small upslope contributing areas (range: 4.21 to 43.2 km^2) and considerable erosion (volume eroded material: 2.8×10^7 to 259×10^7 m^3) when compared to THV that were generated by megafloods elsewhere (upslope contributing area: 228 to 4713 km^2; volume eroded material: 9.2×10^6 to 1.46×10^7 m^3; Lamb et al., 2008; Table 3).

4.3.2 High structural control

In this section, we demonstrate that structural control on the THV in the Sahara can be recognized on two levels. On the regional scale, major, sub-vertical, deep-seated fault systems act as conduits for ascending groundwater, provide opportunities for on- or near-surface discharge, and create a free face that could develop into an escarpment with progressive dissolution and/or denudation of the faulted blocks (Laity, 1988; Luo et al., 1997). On the local scale, fracture systems exert substantial control over the distribution and geometry of the THV. Often the case the THV propagate preferentially along existing fracture planes that represent zones of weakness (Laity and Malin, 1985).

Table 1

Our field observation in the Western Desert in general, and in the four geomorphological sites in particular, together with the inspection of Google Earth images, geological maps (Klitzsch et al., 1987; El-Hinnawi et al., 2005, 2006), and 2D and 3D seismic profiles (Wescott et al., 2011) reveal two prominent, yet poorly understood, fault systems across large sectors of the Western Desert. The first is a northeast-southwest to east-west trending system that could be part of the Pelusium System, a major transcurrent Precambrian fault system that witnessed periodic activities throughout the geologic record (Neev et al., 1982). It runs subparallel to eastern margin of the Mediterranean, curves northeast-southwest across central Africa, and extends from the Nile Delta to the Niger Delta (Neev and Hall, 1982).

The second trend is a northwest-southeast fault system that we interpret here as possibly being reactivated Najd faults. The Najd is the largest Proterozoic transcurrent fault system on Earth (Stern, 1985). It extends for 1200 km in outcrop in the Arabian Peninsula and for an additional 800 km under the sedimentary cover in the Arabian Peninsula, making a potential total length in excess of 2000 km (Brown and Coleman, 1972). Using a pre–Red Sea rift reconstruction, together with field, geochemical, and geochronological data, Sultan et al. (1988and 1993) mapped the extension of the Najd shear system of the Arabian Shield into the basement complex of the Central Eastern Desert of Egypt. We speculate that this system extends at depth under the sedimentary cover in the Eastern and Western Deserts. As is the case with many of the Najd faults in the Eastern Desert that were reactivated by dip slip movement during the Red Sea opening (Sultan et al., 2011; Abotalib and Mohamed, 2013), we suggest that similar movements could have occurred on these faults in the Western Desert. Additional structural trends include the east-west trending Kalabsha dextral faulting in southern parts of the Western Desert (Issawi, 1982; Rayan et al., 2010) and the east-west trending Syrian arc folding and

Table 1

faulting tectonics in the northern parts of the Western Desert (Guiraud and Bosworth, 1997; Kuss et al., 2000). The above-mentioned systems include deep-seated faults (Guiraud and Bosworth, 1997; Saleh, 2011) that witnessed one or more episode of movement throughout their geologic history (Moustafa, 2002; AlFarhan et al., 2006). We suggest that many of these faults acted as conduits for ascending Nubian groundwater.

Spatial correlation (in a GIS environment) of the distribution of THV and the escarpments with the distribution of deep-seated structures in the Western Desert (Fig. 9) extracted from over 700 wells, 2D and 3D seismic profiles (Wescott et al., 2011), satellite and field-based regional structures (Neev et al., 1982; Klitzsch et al., 1987; El-Hinnawi et al., 2005, 2006) revealed the following. First, the boundaries of the Qattara depression, especially the northern Qattara escarpment, is highly dissected by THV; the extension of the northern escarpment correlates largely with the distribution of deep-seated northeast-southwest trending faults, and to a lesser extent with the northwest-southeast trending faults, suggesting a causal effect (Fig. 9A). Second, numerous THV and tufa deposits are observed along Wadi El-Medawara embayment in the Kharga depression; the wadi is bound by deep-seated, east-west trending faults as evidenced by gravity and borehole data (Zaher et al., 2009) that displaced underlying successions including the basement (Hermina, 1990; Thurmond et al., 2004) (Fig. 9B). Third, the western, eastern, and northern escarpments of the Farafra depression are highly dissected by THV and are apparently controlled by the distribution of deep-seated northeast-southwest and northwest-southeast fault systems (Klitzsch et al., 1987; El-Hinnawi et al., 2006; Sanz-Montero et al., 2013) (Fig. 9C). Fourth, the distribution of large-scale THV in the Dakhla depression (Fig. 9D) is typically correlated with the distribution of major faults (northeast-southwest and to a lesser extent by northwest-southeast trending faults; El-Hinnawi et al., 2005).

Table 1

Often, it is the case that where these faults intersect the escarpment, embayments and promontories are formed along the extension of these faults, as with Wadi El-Battikh and Darb El-Tawil (Fig. 9D). Fifth, the structural control over the distribution of the THV is observed on the local level as well. For example, in the Farafra (Fig. 10A) and the Kharga (Fig. 10B) depressions the THV have apparently propagated along northwest-southeast and northeast-southwest trending structural discontinuities, respectively.

4.3.3 Strong-over-weak stratigraphy

We constructed four stratigraphic cross-sections (Fig. 11) across the selected sites using available geological datasets (Klitzsch et al., 1987; Hermina, 1990; Churcher et al., 1999; El-Hinnawi et al., 2005, 2006), elevation data, and field observations to investigate the morpho-stratigraphic relationships in these locations. The four sites are all characterized by strong massive limestone, capping soft, easily eroded shale and argillaceous sandstone. The Qattara depression cross section (Figs. 9A and 11A; A-A′) is excavated in sedimentary rocks of Tertiary age, including the lower Miocene Moghra Formation and the middle Miocene Marmarica Formation (Said, 1962). The Moghra Formation is mainly composed of sandy and clayey beds, whereas the overlying Marmarica Formation composition ranges from pure limestone to shaly limestone and marl (Said, 1962). Further south, in the deepest region of the depression, the black shale of the Upper Eocene–Oligocene Dabaa Formation is exposed (Aref et al., 2002).

The Kharga depression (Figs. 9B and 11B; B-B′) is floored by Upper Cretaceous Quseir and Duwi Formations and the Upper Cretaceous–Paleocene Dakhla Formation. These sedimentary formations are mainly composed of vari-colored shale and siltstone with calcareous marl, phosphorite, and fine-grained sandstone inter-beds (Hermina, 1990). The embayment of

Table 1

Wadi El-Medawara is floored by the greenish-gray shale of the Paleocene-Eocene Esna Formation (El-Hinnawi et al., 2005). Along the scarp face, the Paleocene fossiliferous and chalky limestone of the Kurkur and Tarawan Formations and the underlying Dakhla Formation are exposed. The surface of the plateau is covered by marine carbonate formations ranging from the Paleocene Garra Formation to the Oligocene Katkut Formation.

The Farafra depression (Figs. 9C and 11C; C-C′) is floored by Upper Cretaceous Khoman and Paleocene Tarawan Formations. The Khoman Formation consists of snow-white to light gray chalky limestone in the northern part of the depression, which gives way to dark gray shale of the Dakhla Formation in the south (Klitzsch et al., 1987; El-Hinnawi et al., 2005). The Tarawan Formation is composed of snow-white chalky limestone that is more compact and harder than the underlying Khoman Formation (El-Hinnawi et al., 2005). Escarpment around the depression is made up of the Upper Paleocene and lower Eocene sequences of the Esna and Farafra Formations, respectively (Hermina, 1990). The Esna Formation occupies the lower part of the escarpments and consists of soft green shale intercalated with marl beds, whereas the Farafra Formation caps the escarpment with argillaceous limestone followed upward by snow-white limestone (Said, 1962).

The Dakhla depression (Figs. 9D and 11D; D-D′) is covered by Upper Cretaceous Nubia group including the Taref Sandstone Formation, the overlying Mut claystone, and the Duwi mudstone Formations (Brookes, 2010). The escarpment of the Abu Tartur Plateau is composed of the Upper Cretaceous–Paleocene Dakhla Formation capped by Paleocene Kurkur and Garra Formations. The Dakhla Formation consists mostly of shale, marl, and clay with calcareous and sandy intercalations (Hermina, 1990); the Kurkur and Garra Formations consist of massive thick-bedded limestone.

Table 1

4.3.4 Abundant denudational landforms and tracers for groundwater activity

Field investigations, together with remote sensing–based landscape analysis (Figs. 12 through 16) were conducted in the Qattara, Kharga, Farafra, and Dakhla depressions in search of denudational landforms that are associated with, and indicative of, groundwater activity. Figs. 12A, 14A, and 15 are 3D models covering the Qattara, Farafra, and Dakhla depressions, respectively. Figs. 13A and 13B are merged Landsat 8 images (15 m resolution) for Wadi El-Medawara embayment. Fig. 12B is a merged ALI image (10 m resolution for the Qattara escarpment. Figs. 14B, 14C, and 16 are field shots from the Farafra and Qattara depressions. Inspection of Figs. 12 through 16 indicates that the investigated sites share many denudational landforms. These include, first, drainage systems that over the bounding limestone Libyan Plateau are minimal to absent, whereas the scarp faces are intensively incised by THV in all four sites. Second, there are THV and sink holes that originate at, and propagate along, major faults; examples include THV and sink holes along the east-west trending escarpment of Wadi El-Medawara embayment (Figs. 13A and 13B) and the sink holes in the northern Qattara depression that developed along a northeast-southwest trending fault that runs parallel to the scarp rim (Wescott et al., 2011) (Fig. 12A). Third, endorheic streams begin at the boundary between the strong and underlying weak rock units. In the Qattara depression, endorheic streams emerge at the boundary between the Marmarica limestone Formation and underlying sandy member of Moghra Formation, and/or between the sandy and shaly members of the Moghra Formation, (Fig. 12B). In the Dakhla depression, they emerge at the boundary between the Garra and/or Kurkur limestone Formations and underlying Dakhla shale Formation (Fig. 15). Fourth, widespread playas deposits are found at the terminations of endorheic streams (e.g., Farafra and

Table 1

Dakhla depressions; Figs. 14 and 15). Lastly, we see the removal of large thicknesses of rock sequences by groundwater discharge during wet periods and by aeolian processes in the interleaving dry periods (Aref et al., 2002). Analysis of digital elevation data along transects A-A′ and B-B′ in Fig. 11 showed that the incision of THV in each of the Qattara and Kharga depressions resulted in the removal of large thicknesses (up to 200 m) of the rock sequences.

Each of the investigated areas has its own peculiar denudational landforms and features. For example, in the northern Qattara depression (Fig. 12), we observe the following: (1) the erosional processes removed the limestone cap rock of the Marmarica Formation and exposed the underlying shaly sandstone of the Moghra Formation within sink holes and excavated THV; (2) extensive inland sabkhas located in scarp-foot depressions, possibly where groundwater table intersected the ground surface in previous wet periods; and (3) abundant features related to extensive salt weathering including tafoni, block disintegration, gypsum veins cutting through stratigraphic sequences, polygonal halite and flaky gypsum crusts, and salt quarries (Fig. 16). These field and remote sensing observations in Qattara are consistent with elevated groundwater table during the previous wet climatic periods in the Sahara that caused intensive salt weathering, erosion, and removal of the limestone caprock and the formation of THV and sinkholes.

In Wadi El-Medawara, the abundance of the structurally controlled THV, sinkholes, and tufa deposits within the valleys (Figs. 9B and 13) are consistent with a model that calls on artesian upward leakage from the underlying NAS along deep-seated faults, causing erosion of the plateau, formation of the embayment, and deposition of tufa. Our findings are supported by the work of Smith et al. (2004a, 2004b), who advocated extensive groundwater activity along Wadi El-Medawara based on the wide distribution of tufa deposits over the Paloecene-Eocene units (Smith et al., 2004a, 2004b) and that of Luo et al. (1997) who reported numerous

Table 1

structurally controlled, groundwater sapping-related THV from El-Rufuf Pass, some 80 km to the north.

Our investigations in the Farafra depression revealed abundant denudational and dissolution landforms and remnant hills (e.g. pinnacles, limestone towers, and inselbergs) and sub-parallel ridges (e.g. interfluves) that originate at scarp foothills and extend away from it across a pediment surface. These relationships are observed locally on a 3D model (Fig. 14A) for the Qass Abu Said Plateau at the northwestern corner of the Farafra depression and regionally on Google Earth Digital Globe imagery and Radarsat-1 images (Fig. 7). Along the western escarpment of the Farafra depression, a wide (width: 2.5 km) pediment is observed with extensive west-to-northwest trending subparallel ridges (average height: 3 m; average width: 50 m) separated by interleaving endorheic streams. The ridges originate at, or are proximal to, the scarp face, and transition into a series of rounded remnant hills along their extension away from the scarp face (Figs. 14B and 14C). The origin of these rounded hills was attributed to expulsion of formation water along layer-bounded polygonal fault systems in the Khoman Formation and subsequent preferential fluvial and aeolian erosion along the faulted and fractured surfaces (Tewksbury et al., 2014). Our field observations and analysis of satellite images indicate that these rounded features are bound by two of the dominant fault systems of the Western Desert, the northwest- and northeast-trending faults suggesting a causal effect. We suggest an alternative, yet similar hypothesis: rising groundwater during previous wet climatic periods accessed deep-seated faults and fractures, fluvial and later aeolian erosion along planes of weakness shaped the landscape giving rise to THV at the scarp face, subparallel ridges separated by interleaving endorheic streams, and a series of rounded remnant hills along their extension transitioning away from the scarp.

Table 1

Examination of a 3D model for the Teneida playa basin and Abu Tartur escarpment in the Dakhla depression reveals that small-scale THV or gullies are subdivided in three segments head alcoves, channels, and depositional aprons (Fig. 15). The head alcoves are eroded depressions along the side of a cliff or scarp face, and the depositional aprons are, wedge-shaped features located at the bottom of a hillside; the aprons comprise colluvial and slope wash processes sediments, cut through Pleistocene slumping colluvium along the scarp rampart and terminate in playas at the scarp-foot depression (also see Fig. 6). Detailed field studies identified the slumping colluvium as gravel deposits formed along the scarp ramparts by cliff-sapping of the limestone caprock (Churcher et al., 1999; Kieniewicz and Smith, 2009; Brookes, 2010). The landforms described here bear striking similarities to those observed on the surface of Mars (Malin and Edgett, 2000), which are believed to have been formed by subsurface fluid seepage, followed by surface runoff along slope surfaces.

4.4 Lithologic and isotopic characteristics of playa and tufa deposits

In this section we show that many of the playa and tufa deposits that are proximal to the escarpments have lithologic characteristics and isotopic compositions that are consistent with their deposition from NSAS-related groundwater discharge.

4.4.1 Lithologic characteristics of playa deposits

Inspection of Figs. 3, 6, and 7 indicates that the majority of the reported playa occurrences fall in one of two groups: Group I are found within scarp-foot depressions along linear trends that run parallel and proximal (<25 km) to scarp faces, whereas Group II are distant (>25 km) from the scarp faces and proximal to the west-east trending paleo-channel network

Table 1

(Fig. 7). The unclassified playas on Fig. 7 are found in areas where encroaching thick sand sheets obscure field relations that are here used for classification purposes. The aforementioned observations are consistent with the deposition of Group II playas from the west-east trending paleo-channel network (Fig. 7) and Group I playas from spring waters emerging from the Libyan Plateau escarpments, a suggestion that is supported by the lithologic and isotopic composition of Groups I and II.

Group I playa deposits are characterized by sequences with high carbonate content including intercalated calcareous silty sediments, highly fossiliferous lacustrine marl deposits, fossiliferous authigenic calcite silts, calcareous playa mud deposits, and massive limestone sequences, whereas Group II playa deposits are largely composed of beach gravels, aeolian sand, clay, non-calcareous medium sand, and siliceous mud; authigenic chemical precipitates are absent. Group I playa sequences were reported from the Dakhla depression (Churcher et al., 1999; Kieniewicz and Smith, 2009; Brookes, 2010), Wadi El-Midawara in the Kharga depression (Kieniewicz and Smith, 2007), from Abu Nuss, Ain El-Raml, Bahr, Sheikh El-Obeiyid, and the Bir-Karawein area in the Farafra depression (Hassan et al., 2001; Wanas, 2012; Hamdan and Lucarini, 2013). Group II deposits were reported from the Nabta (Wendorf and Schild, 1980), Bir Kiseiba (Wendorf et al., 1984), Bir Sahara (Szabo et al., 1995), Umm Akhtar (Nicoll, 1998), Darb Al-Arba'in (Haynes, 2001), and Bir Safsaf palyas (Fig. 3; Paillou et al., 2003).

The high carbonate content and relatively high $\delta^{13}C$ (range $\delta^{13}C$: −2.19 to 0.2‰) of the inorganic deposits of Group I playa in the Farafra, Kharga, and Dakhla depressions are consistent with dissolution of limestone by spring waters emerging from the Libyan Plateau escarpment and re-precipitation of calcite within proximal playas (Kieniewicz and Smith, 2007; Kieniewicz and

Table 1

Smith, 2009; Wanas, 2012). Differences in pattern of distribution, distance to escarpments and major streams, calcium carbonate content, and $\delta^{13}C$ values point to differences in water sources between the spring-fed Playa I (Group I) and river-fed Playa II deposits (Group II).

4.4.2 Isotopic analysis of tufa deposits

We conducted the following steps to test whether the isotopic composition of the tufa deposits is consistent with deposition from NSAS fossil groundwater. We first compiled the reported isotopic compositions (Crombie et al., 1997; Sultan et al., 1997; Smith, 2001; Jimenez, 2014) of tufa deposits (147 samples) collected from five localities (Crystal Mountain, Farafra depression, Kharga depression, Kurkur Oasis, and Dakhla depression; Fig. 3) in the Western Desert and used these compositions to derive the isotopic composition ($\delta^{18}O$) of groundwater from which these tufa were deposited. We followed the procedures described in Friedman and O'Neil (1977) for the fractionation of ^{18}O between $CaCO_3$ and water under equilibrium conditions:

$$1000 \ln\alpha = 2.78(10^6 T^{-2}) - 2.89 \quad (2)$$

$$\alpha = (1000 + \delta^{18}O_{calcite})/(1000 + \delta^{18}O_{water}) \quad (3)$$

Where α is the fractionation factor,

T is the prevailing paleo–mean annual air temperature (MAAT, in Kelvin) during calcite deposition from spring water.

$\delta^{18}O_{calcite}$ is the isotopic composition of the tufa, and

$\delta^{18}O_{water}$ is the isotopic composition of the tufa-depositing groundwater

Table 1

The average value (19.8 °C) for the reported (Abouelmagd et al., 2014) noble gas recharge temperatures (NGRT; range: 17.5–22.0 °C) for fossil NSAS in Sinai was used as a proxy for the MAAT.

The composition of the majority of the tufa (118 samples; 80% reported analyses) are consistent with deposition from depleted Nubian waters (range $\delta^{18}O$: −12.8 to −8.0‰) (Patterson et al., 2005). Few samples (29 samples) yield more enriched water compositions (range $\delta^{18}O$: −7.9 to −3.9‰); such enrichments could be attributed to evaporation, degassing, and kinetic effects (Smith et al., 2004a).

Our findings pertaining to the origin of tufa deposits by natural discharge are consistent with those advocated by Nicolle et at al., (1999); they stated that topographic locations, structural morphologies (e.g., wedge-shaped slopes and broad sheets), mineralogical composition (e.g., very high calcite [>90 mol %] and very low $MgCO_3$[<1.2 mol %]), and organo-sedimentary laminations of tufa deposits from different localities near the Kharga depression is indicative of precipitation by processes operating within freshwater spring-fed alkaline stream environments during pluvial Quaternary periods.

4.5 Isotopic analysis of groundwater samples

The main water-bearing horizons in the north Western Desert include six aquifers: the NAS, the carbonate aquifer, the Oligocene aquifer, the Miocene Moghra aquifer, the Pliocene Wadi El-Natrun aquifer, and the Quaternary aquifer (RIGW, 1992). The Oligocene, Miocene, Pliocene, and Quaternary aquifers in the study area (Fig. 17A) are hydrologically connected and are considered as one hydrological unit (REGWA, 1990), hereafter referred to as the Oligocene

Table 1

Miocene Pliocene Quaternary (OMPQ) aquifer. The NAS is separated from these aquifers by the Paleocene-Eocene carbonate aquifer (RIGW, 1992). The NAS was recharged by direct precipitation over its outcrops in southern Egypt and northern Sudan from an Atlantic moisture source during the Pleistocene pluvial periods (Sultan et al., 1997; Sturchio et al., 2004).

The OMPQ aquifer is believed to be largely recharged by groundwater flow from the Nile aquifer with contributions from the underlying aquifers (Thompson, 2007; El-Gamal, 2005), whereas modern recharge from local storms is negligible (<1% total annual recharge) (REGWA, 1990). The suggestion that the OMPQ aquifer is being recharged by groundwater flow from the Nile aquifer is supported by the progressive increase in radiocarbon ages of groundwater samples (31, 33, 61, and 62; Figs. 17B and C) along the general groundwater flow direction (northeast to southwest; RIGW, 1992); we collected our samples from the OMPQ aquifer along two northeast-southwest trending transects proximal to, and west of, the Nile Delta (Figs. 17B and C). Similar findings were reported along an east-to-west transect where an increase in groundwater ages was detected from tens of years in areas proximal to the Nile Delta to thousands of years some 100 km to the west of it (Fig. 17D; samples 8 and 10: <30 YBP; sample 25: 9250 YBP); these ages were estimated using SF_6, ^3H-^3He, and ^{14}C dating methods (Aeschbach-Hertig et al., 2007).

We collected groundwater samples from the Pliocene (six samples), Miocene (four samples), and NAS (10 samples) aquifers, analyzed them for their O and H isotopic compositions, and compared our analyses to reported data (51 samples) from the OMPQ aquifer (Fig. 18). The investigated samples could be classified into four groups on the basis of their isotopic composition. Group I samples were collected from wells tapping the NAS in the Bahariya Oasis, and they have depleted δD and $\delta^{18}O$ values (δD: −84.4 to −80.0‰; $\delta^{18}O$: −10.3 to −11.0‰) similar to those reported from the fossil Nubian groundwater elsewhere (δD: −81 to

Table 1

−72‰; and $\delta^{18}O$: −12.8 to −8.0‰; Sonntag et al., 1978; Sultan, 1997; Patterson et al., 2005). Group II samples were extracted from the OMPQ aquifer; their isotopic composition is enriched (δD: −0.7 to 7.2‰; $\delta^{18}O$: −1.13 to 1.20‰) compared to Group I samples and is similar to that of the pre-High Dam Nile water (δD =−1 to 7.5‰ and $\delta^{18}O$ = −1 to 1.5‰; El-Bakri et al., 1992; Dahab et al., 1999; Sultan et al., 2000) . Our data supports recharge of the OMPQ aquifer by groundwater flow from the Nile Quaternary aquifer.

Not all of the OMPQ aquifer samples have isotopic compositions similar to those of the pre–High Dam. Many of them (19 samples, hereafter referred to as Group III samples) display a wider range of compositions (δD: −62.6 to −2.6‰; $\delta^{18}O$: −7.0 to −1.09‰); Group III samples are here interpreted as being mixtures of fossil Nubian Group I, pre–High Dam Nile Group II, and post–High Dam (Group IV) end members. The samples from Group IV have the highest δD and $\delta^{18}O$ values (δD: 18.8 to 25.4‰; $\delta^{18}O$: 2.08 to 3.10‰) compared to those of Groups I, II, and III, and were collected from the Quaternary aquifer adjacent to the Nile Delta. Group IV samples show a deviation from the global meteoric water line (GMWL) suggesting evaporation-enrichment relationships for ^{18}O and δD.

Inspection of Figs. 17 and 18 shows that the spatial distribution of Group II and III samples do not depend on the distance from the Nile aquifer water. Some of Group III samples are closer to the Nile aquifer than Group II samples. One explanation for this observation is that the fossil Nubian groundwater ascends along deep-seated fault systems and discharges into the shallower OMPQ aquifer. Artesian upward leakage of the deep Nubian waters into the shallower carbonates and alluvium aquifers along deep-seated structures was also reported in the Gulf of Suez (Sturchio et al., 1996) and in the Eastern Desert of Egypt at Wadi El-Asyuti (Sultan et al., 2007) (Fig.1).

Table 1

4.6 Section findings

Our observations and findings are consistent with elevated groundwater levels in the NSAS during previous wet climatic periods and favor a groundwater origin rather than a surface runoff origin for the THV in the Sahara. These statements are supported by the following: (1) LR model outputs over the NSAS reveal an extensive distribution of THV along the escarpments bounding depressions in the Libyan Plateau; (2) spatial analysis of modeled THV reveals strong spatial correlation with the distribution of tufa and Group I playa deposits; (3) analysis of Radarsat-1 and DEM-based stream networks indicates that the well-developed exorheic drainage systems are absent over the Libyan Plateau and that the onset of endorheic streams are associated with the delineated THV; (4) mass balance calculations indicate that the small size of the upslope contributing areas for the individual THV is inconsistent with a fluvial origin for these features given the extensive erosion that is required to remove the large volumes of material that once resided within the area occupied by the THV; (5) areas with abundant THV demonstrate high regional and local structural control; (6) the escarpments that are strongly dissected by THV are characterized by strong-over-weak stratigraphy and show evidence of salt weathering, dissolution features, and groundwater activity; (7) playa deposits proximal to THV within scarp-foot depressions have high carbonate content and are enriched in $\delta^{13}C$ values; (8) isotopic composition ($\delta^{18}O$) of tufa deposits (147 samples) are consistent with deposition from depleted Nubian waters (range $\delta^{18}O$: −12.8 to −8.0‰); and (9) stable isotopic analyses of groundwater samples (71 samples) from the OMPQ aquifer indicate that the fossil Nubian groundwater ascended along deep-seated fault systems and discharged into the overlying shallower OMPQ aquifer.

Table 1

5. DISCUSSION AND IMPLICATIONS

In this section, we first review the popular models (sapping versus surface runoff) that address the origin of the THV and show that the requirements for the former model, not the latter, are available in the study area. We then provide a conceptual model to explain how our preferred sapping model can account for the observed and/or reported topographic, geomorphologic, and hydrogeologic characteristics of the NSAS study area. Finally, we demonstrate the resemblance of the THV over the NSAS to those observed in neighboring Saharan and Arabian fossil aquifer systems, in similar settings world-wide, and on the Martian landscape as well.

5.1 Groundwater versus surface runoff models

The role of groundwater sapping in shaping THV in resistant bedrock has been recently challenged, and alternative models (e.g. megaflooding, waterfall erosion, and landslides) for the development of THV were proposed (Lamb et al., 2006, 2008; Lamb and Dietrich, 2009; Craddock et al., 2012; Lamb et al., 2014; Marra et al., 2014; Irwin et al., 2014). The major arguments they cite against the seepage erosion origin are the bedrock strength and the large size of THV, which necessitate gigantic water discharge systems and/or substantial weathering along the seepage face to disintegrate the bedrock into loose debris and a transporting agent/or agents to remove the debris out of the valley (Howard and Kochel, 1988; Lamb et al., 2006; Luo and Howard, 2008). It also requires a long timescale of groundwater seepage (Howard and Selby, 1994; Lamb et al., 2006).

Table 1

Our findings indicate that the requirements (i.e., prolonged groundwater seepage and a mechanism to disintegrate and transport debris) for the groundwater sapping model, but not the surface runoff model, are present in the study area and that the aforementioned arguments against the groundwater sapping model are not applicable to the Saharan THV.

Our field investigations revealed that strong-over-weak stratigraphy and extensive salt and chemical weathering is common in areas where THV were reported (refer to sections 4.3.3 and 4.3.4), as did the investigations by other researchers in the Qattara depression (Aref et al., 2002), Fayum depression (Keatings et al., 2007), Dakhla depression (El Kammar and El Kammar, 1996; Brookes, 2010), Kharga depression (Salman et al., 2010), and in Egypt's cultural heritage sites such as the Giza Pyramids and Sphinx (Goudie, 2013) and the Pharaonic sandstone monuments in Luxor (Smith, 1986; Wust and Schluchter, 2000). We advocate that the strong-over-weak stratigraphy along with the extensive salt and chemical weathering facilitate the removal of the basal unit along the Saharan escarpments and the development of THV.

The distribution of denudational landforms (refer to section 4.3.4; Figs. 13–16) and the ages (50 to 620 ka of tufa deposits along scarp faces and within scarp-foot depressions; Sultan et al., 1997; Smith et al., 2004a; Adelsberger and Smith, 2010; Jimenez, 2014) suggest that the denudational activities were widely distributed and that they operated for long periods. If the groundwater-related denudational activities operated for a long time span, and if the tufa were deposited from the groundwater, the ages of the groundwater should be consistent with these suggestions; ^{81}Kr and ^{36}Cl groundwater ages (200 ka to 1.2 Ma: Sturchio et al., 2004; Patterson et al., 2005) for 25 samples from the Western Desert show that this is indeed the case. We suggest that fluvial denudational activities operated for long periods during previous wet periods that extend as far back as 1 million years ago. Recent ^{36}Cl ages (up to 1.3 Ma) for groundwater

Table 1

samples from the NSAS (Mohamed et al., 2015) indicate that the denudational activities could have operated for even a longer time period. Our suggestion is supported by the findings from quantitative models that suggest that groundwater processes may have an important role in the development of THV through a combination of seepage weathering and episodic removal of weathered debris by runoff and spring discharge (Pelletier and Baker, 2011). These models were developed to investigate the role of groundwater seepage in weathering bedrock, transporting unconsolidated debris and incision of U-shaped valleys in water-limited environments such as the Sahara.

Extensive sand dune fields are observed in the downwind direction of the Qattara depression (refer to section 4.3.4; Fig. 9A); the composition (quartz sand with minor carbonate, argillaceous material, and gypsum fragments) of the dune material is consistent with derivation from the Moghra and Marmarica Formations cropping along the northern escarpment of the Qattara depression (Aref et al., 2002). We suggest that during the previous wet period, this material could have originated as debris excavated from the Qattara escarpment by groundwater discharge, been transported down the gradient towards the depression floor, and been disintegrated by salt weathering and later deflated by winds in subsequent dry periods. This suggestion is supported by the findings of Brookes (2001, 2003), who emphasized the role of aeolian erosion in shaping landscapes, carving depressions, and transporting unconsolidated debris during the interleaving dry periods in the Egyptian portion of the Sahara.

We suggest that the oscillation of the wet and dry climatic conditions (Szabo et al., 1995; Smith et al., 2004a) over the Sahara probably accelerated the scarp retreat. During wet periods, rock falls and slumped blocks accumulate along the ramparts and are partially eroded by the endorheic fluvial drainage systems originating from the scarp faces, and are disintegrated by salt

Table 1

weathering processes. With the advent of aridity, the groundwater table is lowered, wind activity intensifies, and additional weathered and disintegrated debris is removed by deflation from the valley floor. Groundwater sapping activities increase the rate at which escarpments retreat (Higgins and Osterkamp, 1990). Throughout the past 620,000 years, the retreat of the eastern escarpment bounding the Southern High Plains in Texas was rapid (190 m/1000 yr) (Simpkins and Baumgardner, 1982), compared to the northern escarpment (31 to 42 m/1000 yr) (Gustavson et al., 1980). The former, but not the later area, is highly affected by sapping processes. If we were to adopt the Southern High Plains rates in the Western Desert, we estimate that the escarpment could have retreated by some 200 km in a million years, a distance that exceeds the width of each of the Farafra (maximum width: 75 km) and Qattara depressions (maximum width: 176 km). The scarp retreat in the Dakhla and Kharga could not be estimated given that they are open depressions, unlike the closed Farafra and Qatarah depressions. We suggest that the continuous processes of groundwater discharge, scarp retreat, and sediment transport in wet and dry periods are responsible for the formation of THV and the excavation of the natural depressions.

The features cited in support of surface runoff models (i.e., maegaflooding or waterfall erosion) for the origin of the THV in the Box Canyon and Malad Gorge, Idaho and in Hawaii (Lamb et al., 2008, and 2014; Craddock et al., 2012) are absent in the study area. These models require the presence of large watersheds that collect extensive amount of precipitation and channel them into a limited number of valleys. We have shown that the distribution of the NSAS THV is extensive along the length of the scarp, there is a general lack of well-developed watersheds draining into the THV, and if present they are limited in size (typically <15 km^2; refer to section 4.3.1). The surface runoff models are more suited for areas of high to medium

Table 1

slope gradients, where infiltration is minimal and runoff is high. That is not the case in the study area, where the flat-topped limestone plateau occupies large sectors of the NSAS landscape (refer to section 2). Moreover, there are no records of megafloods during the Quaternary period in the study area.

5.2 Conceptual Model

We developed a conceptual model based on our findings to assess the origin of THV and natural depressions in the study area, and possibly across the Sahara (Fig. 19). Seven stages are suggested: (1) precipitation over the Nubian sandstone outcrops in the south (i.e., the NAS) during the previous wet climatic periods resulted in a considerable rise of the paleo-piezometric surface as much as 25 m higher than the present level (Pachur and Hoelzmann, 2000); (2) further to the north, the thick sedimentary sequences (up to 2 km thick), the confined nature of the aquifer, and the presence of deep-seated sub-vertical faults led to upward migration of groundwater from the NAS to discharge at or near the surface; (3) groundwater flow converged along free faces either formed by structural discontinuities (e.g., faults or shear zones) or to a lesser extent by hydraulic piping failures; (4) small THV originate along free faces and enlarge and deepen with continued discharge of groundwater giving rise to extensive denudation along the structurally controlled escarpments; (6) the massive carbonate caprock is undermined and slumps, and the escarpment recedes by continued groundwater seepage along the contact between the limestone caprock and the underlying weak units and by seepage weathering of rock debris; and (7) rock debris is removed from the ramparts of the escarpment either by fluvial processes in wet periods or by wind erosion during arid periods. These stages give rise to the

Table 1

following landforms: THV, natural depressions, circular remnant hills, sabkhas, spring mounds, and endorheic paleolakes.

The model we advocate here introduces a regional comprehensive solution for the enigmatic occurrence of natural depressions and associated landforms over the Libyan Plateau in the Sahara and overcomes the shortcomings of the previous models. Models that call on the formation of natural depression by wind deflation encounter difficulties explaining the removal of massive limestone caprocks across the Sahara by wind alone. The proposed model can. As indicated earlier, in wet periods, rising groundwater compromises the integrity of the caprock; it removes underlying soft beds, causing rockfalls and block slumping of caprocks and its disintegration by salt weathering and dissolution. Caprock debris is further weathered and removed by wind deflation in interleaving arid periods. Models that call on the formation of natural depressions by fluvial stream erosion cannot explain the absence of well-developed exorheic streams over the Libyan Plateau. The groundwater sapping model does not require the existence of surface exorheic streams where the driving force is ascending groundwater. Our model explains the role of endorheic streams, seepage weathering, and/or wind erosion in the removal of rock falls on the scarp ramparts, deposition of tufa along scarp faces, development of landforms within scarp-foot depressions, and deposition of high calcium carbonate sediments within paleolakes.

5.3 Regional and planetary implications

We applied the procedures that were used to identify and map the THV over the NSAS to investigate the presence of these valleys over other fossil aquifer systems in the Sahara and in the Arabian Peninsula. Specifically, we applied the morphological characteristics (10 characteristics:

Table 1

refer to sections 2 and 4.1.1) and statistical analysis (refer to section 4.1). Our analysis revealed extensive occurrence of THV along, or proximal to, escarpments that we interpret as paleo-discharge locations in the Saharan and Arabian Deserts. We cite two examples, the NWSAS and the Upper-Mega Aquifer System in the Plateau of Najd in Saudi Arabia (Figs. 1, 20A, 20B). Our findings and those reported in the literature indicate that the THV in these two aquifer systems share remarkable geologic, hydrologic, and geomorphologic characteristics with those reported from the NSAS. These include: (1) local structural control along pre-existing structural discontinuities (e.g., propagation directions that are northeast-east parallel to the main trend of the Gebel El-Gharbi escarpment; Figs. 20A and 20C); (2) minimal upstream contribution areas for many of the THV; they are typically <50 km^2 in size (e.g., NWSAS, Gebel El-Gharbi area; Fig. 20C) and in some cases, they are absent as is the case with the Tuwaiq Mountains (Fig. 20B) in the Najd Plateau where the Plateau dips steeply towards the east and away from the main valley propagation direction to the west (Fig. 20D); (3) the THV, escarpment, and deep-seated faults are within the confined sectors of the aquifer where clastic-dominated formations are overlain by thick carbonate and shale deposits (Thorweihe and Heinl 2002; Edmunds et al., 2003; Stöckl, 2010); (4) THV are located within areas that witnessed wet climatic periods, elevated groundwater levels in the Pleistocene (Causse et al., 1989; McLaren et al., 2009), and natural discharge of fossil groundwater (>1 million years (Guendouz and Michelot, 2006; Sultan et al., 2015) along deep-seated sub-vertical faults (Swezey, 1996; Engelhardt et al., 2013) and within areas of high structural control (Cornet, 1964; Guendouz and Michelot, 2006; Beaumont, 1977).

The widespread distribution of the THV in the NSAS (1450 km; refer to section. 4.1.2), the NWSAS (~1500 km along the Hamada De Tinhert, Plateau De Tademait, and Gebel El-

Table 1

Gharbi escarpments; Fig. 20A), and the Najd Plateau (~500 km along the Tuwaiq mountain escarpment; Fig. 20B) suggest extensive and widespread groundwater discharge and intense groundwater denudational activities in the Saharan and Arabian deserts during the previous wet climatic periods.

Similar groundwater-related denudational processes and/or landforms (i.e., sapping features, headward channel growth, scarp retreat, and incised canyons) were reported from many areas outside of the Saharan and Arabian deserts. Examples include, the extensive landscape modifications in the northern China deserts by progressive headward channel growth of THV (Yang et al., 2015), the retreat of the Southern High Plains (Wood, 2002), the undermining of the massive Navajo Sandstone in the Colorado Plateau and the integration of the Colorado River system (Laity and Malin, 1985; Crossey et al., 2015), and the incision of canyons within plateaus (Hackness Hill Plateau, England: Nash, 1996; Murge Plateau, Italy: Mastronuzzi and Sanso, 2002; Altiplano Plateau, northern Chile: Hoke et al., 2004).

Extensive and widespread THV (outflow channels) were recorded on Mars along the length of, and cutting across, the walls of Valles Marineris (Marra et al., 2015; Fig. 21). Understanding the Martian surface and subsurface processes and their effects on the evolution of the landscape is hindered by the inaccessibility of Mars. Fortunately, the hyper-arid Sahara provides one of the best terrestrial analogs for examining the origin and evolution of many of the Martian landscape features (Higgins, 1982; Grant et al., 2004; Paillou et al., 2014), especially THV. The individual THV on Mars are larger in size than their Arabian and Saharan counterparts, yet they are geomorphologically similar (Higgins, 1982; Luo, 2000) (Fig. 21, inset). The Martian THV display characteristics similar to those reported from their Saharan and Arabian counterparts: (1) they are widespread and densely distributed along the length of

Table 1

Martian escarpments for over 1400 km (Marra et al., 2015), (2) they are located largely in areas where extensive faulting was reported (Treiman, 2008; Montgomery et al., 2009), a suggestion that is supported by the distribution of many of the THV along linear structural discontinuities, (3) they lack well-developed stream networks draining towards the individual THV (Fig. 21), and (4) they are frequently associated with large-scale spring deposits (Rossi et al., 2008), but lack flood deposits commonly associated with terrestrial THV that are generated by megafloods (McEwen et al., 2012). The occurrence of these features along the crest of a 3 km high topographic bulge on the Tharsis Plateau (Montgomery and Gillespie, 2005), their dense distribution, their presence along both sides of Valles Marineris on surfaces dipping away from the canyon, and the general absence of large drainage areas needed to form individual Martian THV (Fig. 21) makes it unlikely that they originated from well-developed exorheic systems.

Given the above mentioned observations from the Tharsis Plateau, the similarities between the Saharan and Martian THV, our findings pertaining to the significant role of groundwater processes in shaping the Saharan landscape, and the reported gigantic groundwater discharge on Mars (Montgomery and Gillespie, 2005; Montgomery et al., 2009; Mara et al., 2015), we suggest that future studies should investigate: (1) the potential role of structural control, pressurized groundwater discharge, and sapping processes in the evolution of the Martian landscape, and (2) the origin of the recently reported recurring slope lineae (McEwen et al., 2014) on the slopes of Valles Marineris.

6. ACKNOWLEDGMENTS

This study was partially supported by the Egyptian Ministry of Higher Education and Scientific Research and by Western Michigan University (Gwen Frostic Doctoral Fellowship and Earth

Table 1

Sciences Remote Sensing Facility). We thank the editor and reviewers of the Earth-Science Reviews, for their instructive comments and suggestions, Professor Mamdouh Abdeen for his assistance and support, and the National Authority of Remote Sensing and Space Sciences (NARSS) in Egypt for providing logistical support for travel and field work.

FIGURE CAPTIONS

Fig. 1. Location map. (A) Hillshade map for the study area in the Western Desert of Egypt and northern Sudan showing the distribution of depressions and sample locations for O and H isotopic analyses (yellow circles). Open red boxes outline areas covered by Figs. 3, 6A, 6B, 7, 8A, 8B, 8C, 8D, 9A, 9B, 9C, 9D, 10A, 10B, 12A, 14A, 15, and 17A; solid red boxes outline areas displayed in Figs. 4A, 4B, 4C, 5A, 5B, 5C, 13A, and 13B; transects A-A′, B-B′, C-C′, and D-D′ denote cross sections displayed in Figs. 11A, 11B, 11C, and 11D. Inset shows the location of the study area (Box B) and the distribution of fossil aquifers across North Africa and Arabia.

Fig. 2. Hydrostratigraphy of the NSAS. (A) Sketch map showing the distribution of the NSAS in northeast Africa, distribution of confined and unconfined aquifers (PNAS, NAS) within the NSAS, and the groundwater flow directions. (B) Simplified hydrostratigraphic cross-section along line A-A' plotted on Fig. 2A (modified from Thorweihe, 1990).

Fig. 3. Hillshade map for the study area showing the distribution of playas (El-Hinnawi et al., 2005, 2006), tufa deposits (Smith et al., 2001; Kieniewicz and Smith, 2009; Torab, 2013;

Table 1

Jimenez, 2014), springs (Klitzsch et al., 1987), and our LR model outputs (distribution of modeled THV). Area covered by Fig. 3 is outlined by open red box 2 on Fig. 1.

Fig. 4. Typical features for THV in plain view (*left*) and in cross section (*right*) in the Farafra (3A), Kharga (3B), and Qattara depressions (3C), including stubby-looking geometry, theater-like heads, structural control patterns, a U-shaped profile, Vf values >1, flat floors, and low stream order. Stratigraphic data in cross sections were derived from Klitzsch et al. (1987), Luo et al. (1997), El-Hinnawi et al. (2005; 2006), and field measurements. Areas covered by Figs. 4A, 4B, and 4C are outlined by solid red boxes 4A, 4B, and 4C, respectively, on Fig. 1

Fig. 5. Google Earth images showing selected THV in the Western Desert (*left*) and the LR model-delineated pixels (*red squares*) along the alcoves (*right*) in the Farafra (Fig. 5A), Kharga (Fig. 5B), and Qattara (Fig. 5C) depressions. Areas covered by Figs. 5A, 5B, and 5C are outlined by solid red boxes 5A, 5B, and 5C, respectively, on Fig. 1.

Fig. 6. Color-coded digital elevation model showing the spatial correlation between the distribution of THV-rich escarpments and tufa deposits in the Kharga (Wadi El-Midauwara) (Fig. 6A) and Dakhla depressions (Fig. 6B). The letter T refers to selected locations of THV. Areas covered by Figs. 6A and 6B are outlined by open red boxes 6A and 6B, respectively, on Fig. 1.

Table 1

Fig. 7. Radarsat-1 mosaic over southwest Egypt and northern Sudan showing the distribution of reported playa deposits (El-Hinnawi et al., 2005), LR-delineated THV, and SRTM-delineated major streams. Area covered by Fig. 7 is outlined by open red box 7 on Fig. 1.

Fig. 8. Delineated stream networks over the THV-rich escarpments and the Libyan Plateau showing minimal contribution of plateau surface runoff to depressions and their bounding escarpments in the Qattara (Fig. 8A), Kharga (Fig. 8B), Farafra (Fig. 8C), and Dakhla depressions (Fig. 8D) . Areas covered by Figs. 8A through 8D are outlined by red boxes 8A through 8D, respectively on Fig. 1.

Fig. 9. Distribution of major fault traces, deep-seated faults, and the Pelusium meagashear system (Klitzsch et al., 1987; El-Hinnawi et al., 2005, 2006; Wescott et al., 2011) in the Qattara (Fig. 9A), Kharga (Fig. 9B), Farafra (Fig. 9C), and Dakhla (Fig. 9D) depressions plotted on hillshade images. Areas covered by Figs. 9A through 9D are outlined by open red boxes 9A through 9D, respectively, on Fig. 1. Also shown are locations at which detailed geomorphological studies and stratigraphic cross-sections were conducted in the Qattara (Figs. 1, 9A: box 12A, line A-A′), Kharga (Figs. 1, 9B: boxes 13A and 13B, line B-B′), Farafra (Figs. 1, 9C: box 14A, line C-C′), and Dakhla (Figs. 1, 9D: box 15, line D-D′) depressions.

Fig. 10. Local structural control on the spatial distribution of THV in the Farafra (Fig. 10A) and Kharga (Fig. 10B) depressions. Areas covered by Figs. 10A and 10B are outlined by open red boxes 10A and 10B, respectively, on Figs. 1 and 7 .

Table 1

Fig. 11. Simplified stratigraphic cross-sections across the selected four sites, including the Qattara (Fig. 11A), Kharga (Wadi El-Medawara; Fig. 11B); Farafra (Fig. 11C), and Dakhla (Fig. 11D) depressions showing the strong-over-weak stratigraphy. Stratigraphic data was extracted from Klitzsch et al. (1987), Hermina (1990), and El-Hinnawi et al. (2005, 2006). The cross sections were constructed along transects A-A′, B-B′, C-C′, and D-D′ shown as solid lines on Figs. 1 and 9.

Fig. 12. Denudational landforms along the northern Qattara escarpment. (A) 3D model showing the extensive distribution of THV along the scarp face and the presence of sink holes on the plateau and their alignment with an identified deep-seated fault (Wescott et al., 2011); (B) High-resolution (10 m resolution) ALI image for the area outlined by box B in Fig. 12A showing the emergence of streams at the contact between the limestone Marmarica Formation and underlying sandy member of Moghra Formation, or between sandy and shaly members of the Moghra Formation. The area covered by Fig. 12A is outlined by open box 12A on Figs. 1 and 9, and a T marks the location of selected THV.

Fig. 13. Denudational landforms in the Kharga depression (Wadi El-Medawara embayment). (A) Merged Landsat 8 image showing the distribution of sinkholes along an east-west trending fault (*yellow arrows*) that is part of the Seyal fault system. (B) Merged Landsat 8 image showing the origination and propagation of THV (marked with a T) along a major east-west trending fault

Table 1

that belongs to the Seiyal fault system (Jerris, 2014). Areas covered by Fig. 13A and 13B are outlined by open boxes 13A and 13B, respectively, on Figs. 1 and 9.

Fig. 14. Denudational landforms in the Farafra depression. (A) 3D model for the northwestern escarpment at Qass Abu Said Plateau showing the distribution of denudational and dissolution landforms. (B) Rounded remnant hillocks (inselbergs) of playa deposits in Ain El-Raml area (Fig. 1). (C) Rounded remnant hills (pinnacles) of the chalky limestone Khoman Formation. Area covered by Fig. 14A is outlined by open box 14A on Figs. 1 and 9.

Fig. 15. Three-dimensional model of Teneida playa basin and Abu Tartur Plateau showing the characteristics of THV emanating from Abu Tartur scarp face. Area covered by Fig. 15 is outlined by open box 15 on Figs. 1 and 9.

Fig. 16. Features related to salt weathering in the Qattara depression. (A) Tafoni landform in the Moghra sandstone Formation; (B) block disintegration of the of the Moghra sandstone and spalling of the underlying evaporite vein–rich Moghra shale; (C) halite and gypsum veins cutting through the Moghra shale; (D) gypsum flakes at the boundary between the Moghra sandstone and shale; (E) polygonal-shaped halite crust; (F) ongoing salt quarrying from the sabkha.

Fig. 17. (A) Distribution of groundwater samples from this study (closed symbols) and from previous studies (Thompson, 2007; El-Gamal, 2005) (open symbols) from the Quaternary Nile,

Table 1

Pliocene, Miocene, Oligocene, and NAS aquifers in the north Western Desert of Egypt that were analyzed for their stable isotopic compositions (O and H) and locations of transects along which groundwater samples were collected in this study (T1 and T2) and in previous studies (T3; Aeschbach-Hertig et al., 2007) for ^{14}C dating. Enlargement of areas encompassing T1, T2, and T3 on Fig. 17A are shown in Figs 17B, 17C, and 17D, respectively; these figures show transect location (*purple line*), sample numbers (*yellow*) and C-14 ages (*red*). Area covered by Fig. 17A is outlined by open red box 17A on Fig. 1, and locations of wells are shown as solid yellow circles on Fig. 1.

Fig. 18. δD versus $\delta^{18}O$ plot for groundwater samples from fossil Nubian aquifer NAS (Group I), OMPQ aquifer (Groups II and III), and Quaternary Nile Aquifer Group (IV). Also shown are the fields for the NAS groundwater (Sultan et al., 1997; Patterson et al., 2005), pre–High Dam groundwater (El-Bakri et al., 1992; Sultan et al., 2000), and post–High Dam groundwater (Dahab et al., 1999; El-Gamal, 2005), the GMWL as a solid line ($\delta D = \delta^{18}O+10$; Craig, 1961) and the evaporation line for the Nile water as a dotted line (Sultan et al., 2000).

Fig. 19. Block diagram of the NSAS (modified from Salem and Pallas, 2004) and landscape evolution schematic diagrams showing summary of the proposed hydrological and geomorphological processes leading to the formation of THV and natural depressions in the Sahara.

Table 1

Fig. 20. Distribution of THV in Saharan and Arabian fossil aquifers. (A) Hillshade image showing delineated THV in the NWSAS. (B) Hillshade image showing delineated THV in the Najd Plateau in Saudi Arabia. (C) False-color Landsat 8 data for area C in Fig 20A showing that the THV are structurally controlled by northeast-east trending structural discontinuities and that they receive minimal upstream contributions for the THV. (D) False-color Landsat 8 data for area D in Fig. 20B showing endorheic streams and THV draining to the west in a direction opposite from the dip of the plateau (east) and the drainage direction of the exorheic streams on the plateau (*bright areas*). The letter T marks the onset of the THV.

Fig. 21. Color-coded digital elevation model extracted from the MOLA mosaic for the eastern region of Valles Marineris and surroundings showing extensive and dense distribution of THV (marked with letter "T") and absence of well-developed streams draining toward the THV. Inset: enlargement for area covered by the red box generated from the HRSC mosaic (ESA/DLR/FU Berlin) showing the distribution of THV along the walls of Ius Chasma.

Table 1

REFERENCES

Abdeldayem, A. L., 1996. Palaeomagnetism of some Miocene rocks, Qattara depression, Western Desert, Egypt. J. African Earth Sci. 22, 525-533.

Abotalib, A.Z., Mohamed, R.S.A., 2013. Surface evidences supporting a probable new concept for the river systems evolution in Egypt: a remote sensing overview. Environ. Earth Sci. 69, 1621–1635.

Abouelmagd, A., Sultan, M., Milewski, A., Kehew, A.E., Sturchio, N.C., Soliman, F., Krishnamurthy, R.V., Cutrim, E., 2012. Toward a better understanding of palaeoclimatic regimes that recharged the fossil aquifers in North Africa: Inferences from stable isotope and remote sensing data. Palaeogeogr. Palaeoclimatol. Palaeoecol. 329, 137–149.

Abouelmagd, A., Sultan, M., Sturchio, N.C., Soliman, F., Rashed, M., Ahmed, M., Kehew, A.E., Milewski, A., Chouinard, K., 2014. Paleoclimate record in the Nubian Sandstone Aquifer, Sinai Peninsula, Egypt. Quat. Res. 81, 158–167.

Adelsberger, K.A., Smith, J.R., 2010. Paleolandscape and paleoenvironmental interpretation of spring-deposited sediments in Dakhleh Oasis, Western Desert of Egypt. Catena 83, 7–22.

Aeschbach-Hertig, W., El-Gamal, H., Dahab, K., Friedrich, R., Kipfer, R., Hajdase, I., 2007. Identifying and dating the origin of groundwater resources in reclamation areas of Egypt. Advances in Isotope Hydrology and its Role in Sustainable Water Resources Management, Vienna 395–403.

Akgün, A., Türk, N., 2011. Mapping erosion susceptibility by a multivariate statistical method: a case study from the Ayvalık region, NW Turkey. Comput. Geosci. 37, 1515–1524.

Albritton, C.C., Brooks, J.E., Issawi, B., Swedan, A., 1990. Origin of the Qattara depression, Egypt. Geol. Soc. Am. Bull. 102, 952–960.

Table 1

Alfarhan, M.S., Arafat, S.M., Abdelsalam, M.G., 2006. Interplay of Cretaceous-Quaternary faulting and folding in the south desert of Egypt: Insights from remote sensing analysis, in: Geological Society of America Abstracts with Programs. 3–15.

Aref, M.A.M., El-Khoriby, E., Hamdan, M.A., 2002. The role of salt weathering in the origin of the Qattara Depression, Western Desert, Egypt. Geomorphology 45, 181–195.

Bakhbakhi, M., 2006. Nubian sandstone aquifer system. Non-renewable Groundw. Resour. A Guideb. Soc. Sustain. Manag. Water-Policy Makers, Paris United Nations Educ. Sci. Cult. Organ. (IHP-VI Ser. Groundw. 10), pp. 75–81.

Ball, J., 1927. Problems of the Libyan desert. Geogr. J. 21–38.

Beaumont, P., 1977. Water and development in Saudi Arabia. Geogr. J. 42–60.

Bellin, N., Vanacker, V., Kubik, P.W., 2014. Denudation rates and tectonic geomorphology of the Spanish Betic Cordillera. Earth Planet. Sci. Lett. 390, 19–30.

Brookes, I.A., 2001. Aeolian erosional lineations in the Libyan desert, Dakhla region, Egypt. Geomorphology 39, 189–209

Brookes, I.A., 2003. Geomorphic indicators of Holocene winds in Egypt's Western Desert. Geomorphology 56, 155–166.

Brookes, I.A., 2010. Spatially variable sedimentary responses to orbitally driven pluvial climate during Marine Oxygen Isotope Stage 5.1, Dakhla Oasis region, Egypt. Quat. Res. 74, 252–264.

Brown, G.F., Coleman, R.G., 1972. The tectonic framework of the Arabian Peninsula. 24th International Geological Congress Report, Montreal, 3, p.300-305.

Table 1

Caussé, C., Coque, R., Fontes, J.C., Gasse, F., Gibert, E., Ouezdou, H. Ben, Zouari, K., 1989. Two high levels of continental waters in the southern Tunisian chotts at about 90 and 150 ka. Geology 17, 922–925.

Cherkinsky, A., Culp, R.A., Dvoracek, D.K., Noakes, J.E., 2010. Status of the AMS facility at the University of Georgia. Nucl. Instruments Methods Phys. Res. Sect. B Beam Interact. with Mater. Atoms 268, 867–870.

Churcher, C.S., Kleindienst, M.R., Schwarcz, H.P., 1999. Faunal remains from a Middle Pleistocene lacustrine marl in Dakhleh Oasis, Egypt: palaeoenvironmental reconstructions. Palaeogeogr. Palaeoclimatol. Palaeoecol. 154, 301–312.

Conoscenti, C., Angileri, S., Cappadonia, C., Rotigliano, E., Agnesi, V., Märker, M., 2014. Gully erosion susceptibility assessment by means of GIS-based logistic regression: A case of Sicily (Italy). Geomorphology 204, 399–411.

Cornet, A., 1964. Introduction à l'hydrogéologie Saharienne. Rev. Geéographie Phys. Géologie Dyn. 61, 5–72.

Craddock, R.A., Howard, A.D., Irwin, R.P., Tooth, S., Williams, R.M.E., Chu, P., 2012. Drainage network development in the Keanakāko ʻi tephra, Kīlauea Volcano, Hawai ʻi: Implications for fluvial erosion and valley network formation on early Mars. J. Geophys. Res. Planets 117.

Crombie, M.K., Arvidson, R.E., Sturchio, N.C., El Alfy, Z., Zeid, K.A., 1997. Age and isotopic constraints on Pleistocene pluvial episodes in the Western Desert, Egypt. Palaeogeogr. Palaeoclimatol. Palaeoecol. 130, 337–355. doi:10.1016/S0031-0182(96)00134-4

Crossey, L.C., Karlstrom, K.E., Dorsey, R., Pearce, J., Wan, E., Beard, L.S., Asmerom, Y., Polyak, V., Crow, R.S., Cohen, A. and Bright, J., 2015. Importance of groundwater in

Table 1

propagating downward integration of the 6–5 Ma Colorado River system: Geochemistry of springs, travertines, and lacustrine carbonates of the Grand Canyon region over the past 12 Ma. Geosphere 11,660-682.

Dahab, K., Sadek, M., El-Fakharany, M. K., 1999. Replenishment and mineralization processes of lower Miocene aquifer at Wadi El-Farigh area and its vicinities, using environmental isotopes and hydrochemistry. Sci. J, Fac. Sci. Menufia Univ. 13, 15–25.

Devauchelle, O., Petroff, A.P., Seybold, H.F., Rothman, D.H., 2012. Ramification of stream networks. Proc. Natl. Acad. Sci. USA 109, 20832–20836. doi:10.1073/pnas.1215218109

Dunne, T., 1980. Formation and controls of channel networks. Prog. Phys. Geogr. 4, 211–239. doi:10.1177/030913338000400204

Edmunds, W.M., Guendouz, A.H., Mamou, A., Moulla, A., Shand, P., Zouari, K., 2003. Groundwater evolution in the Continental Intercalaire aquifer of southern Algeria and Tunisia: trace element and isotopic indicators. Appl. Geochemistry 18, 805–822.

Coplen, T.B., 1996. New guidelines for reporting stable hydrogen, carbon, and oxygen isotope–ratio data. Geochim. Cosmochim. Acta 60, 3359–3360.

El-Bakri, A., Tantawi, A., Blavoux, B., Dray, M., 1992. Sources of water recharge identified by isotopes in El Minya Governate (Nile valley, Middle Egypt), in: Proceeding of International Symposium on Isotope Techniques in Water Resources Development 1991, IAEA, Vienna, 643-645.

El-Gamal, H., 2005. Environmental tracers in groundwater as tools to study hydrological questions in arid regions. PhD Thesis, University of Heidelberg, 146 pp.

El-Hinnawi, M., Philibbos, E., Riad, S., El-Khawaga, M.M., 2005. Geological Map of the south Western Desert, Egypt.

Table 1

El-Hinnawi,M., Philibbos, E., Riad, S., El-Khawaga, M.M., 2006. Geological Map of the north Western Desert, Egypt.

El Kammar, A.M., El Kammar Jr, M.M., 1996. Potentiality of chemical weathering under arid conditions of black shales from Egypt. J. Arid Environ. 33, 179–199.

Engelhardt, I., Rausch, R., Keim, B., Al-Saud, M., Schüth, C., 2013. Surface and subsurface conceptual model of an arid environment with respect to mid- and late Holocene climate changes. Environ. Earth Sci. 69, 537–555.

Fernandez, S., Marquínez, J., Menéndez-Duarte, R., 2008. A sapping erosion susceptibility model for the southern Cantabrian Range, North Spain. Geomorphology 95, 145–157.

Friedman, I., O'Neil, J.R., 1977. Compilation of stable isotope fractionation factors of geochemical interest. In: Fleischer. (Eds.), Data of Geochemistry, 6th Ed. Geological Survey Professional Paper 440-KK.

Ghoneim, E., El-Baz, F., 2007. The application of radar topographic data to mapping of a mega-paleodrainage in the Eastern Sahara. J. Arid Environ. 69, 658–675.

Giaconia, F., Booth-Rea, G., Martínez-Martínez, J.M., Azañón, J.M., Pérez-Peña, J.V, 2012. Geomorphic analysis of the Sierra Cabrera, an active pop-up in the constrictional domain of conjugate strike-slip faults: The Palomares and Polopos fault zones (eastern Betics, SE Spain). Tectonophysics 580, 27–42.

Gindy, A.R., Albritton, C.C., Brooks, J.E., Issawi, B., Swedan, A., 1991. Origin of the Qattara Depression, Egypt: Discussion and reply. Geol. Soc. Am. Bull. 103, 1374–1376.

Goudie, A.S., 2013. Arid and semi-arid geomorphology. Cambridge University Press.

Table 1

Grant, J.A., Maxwell, T.A., Johnston, A.K., Kilani, A., Williams, K.K., 2004. Documenting drainage evolution in Bir Kiseiba, southern Egypt: Constraints from ground penetrating radar and implications for Mars. J. Geophys. Res. Planets 109.

Guendouz, A., Michelot, J.-L., 2006. Chlorine-36 dating of deep groundwater from northern Sahara. J. Hydrol. 328, 572–580.

Guiraud, R., Bosworth, W., 1997. Senonian basin inversion and rejuvenation of rifting in Africa and Arabia: synthesis and implications to plate-scale tectonics. Tectonophysics 282, 39–82.

Gustavson, T. C., Finley, R.J., and McGillii, K.A., 1980. Regional dissolution of Permian salt in the Anadarko, Dalhart and Palo Duro basins of the Texas Panhandle. University of Texas at Austin Bureau of Economic Geology, Austin.

Hamdan, M.A., Lucarini, G., 2013. Holocene paleoenvironmental, paleoclimatic and geoarchaeological significance of the Sheikh El-Obeiyid area (Farafra Oasis, Egypt). Quat. Int. 302, 154–168.

Hassan, F.A., Barich, B., Mahmoud, M., Hemdan, M.A., 2001. Holocene playa deposits of Farafra Oasis, Egypt, and their palaeoclimatic and geoarchaeological significance. Geoarchaeology 16, 29–46.

Haynes, C.V., 2001. Geochronology and climate change of the Pleistocene–Holocene transition in the Darb el Arba'in Desert, Eastern Sahara. Geoarchaeology 16, 119–141.

Haynes, C.V., Haas, H., 1980. Radiocarbon evidence for Holocene recharge of ground water, Western Desert, Egypt. Radiocarbon 22, 705–716.

Hermina, M., 1990. The surroundings of Kharga, Dakhla and Farafra oases, in: The Geology of Egypt. Balkema, Rotterdam, pp. 259–292.

Table 1

Higgins, C.G., 1982. Drainage systems developed by sapping on Earth and Mars. Geology 10, 147–152.

Higgins, C.G., Osterkamp, W.R., 1990. Seepage-induced cliff recession and regional denudation. Geol. Soc. Am. Spec. Pap. 252, 291–318.

Hobbs, S.W., Paull, D.J., Clarke, J.D.A., 2014. A comparison of semiarid and subhumid terrestrial gullies with gullies on Mars: Implications for Martian gully erosion. Geomorphology 204, 344–365.

Hoke, G.D., Isacks, B.L., Jordan, T.E., Jennifer, S.Y., 2004. Groundwater-sapping origin for the giant quebradas of northern Chile. Geology 32, 605–608.

Howard, A.D., Kochel, R.C., 1988. Introduction to cuesta landforms and sapping processes on the Colorado Plateau. NASA Spec. Publ. 491, 6.

Howard, A.D., Selby, M.J., 1994. Rock slopes, in: In: Abrahams, A.D., Parsons, A.J. (Eds.), Geomorphology of Desert Environments. Springer, pp. 123–172.

International Groundwater Resources Assessment Centre (IGRAC).2012. Transboundary Aquifers of the World. Available at http://www.un-igrac.org/dynamics/modules/SFIL0100/view.php?fil_Id=213

Irwin, R.P., Tooth, S., Craddock, R.A., Howard, A.D., de Latour, A.B., 2014. Origin and development of theater-headed valleys in the Atacama Desert, northern Chile: Morphological analogs to Martian valley networks. Icarus 243, 296–310.

Issawi, B., 1982. Geology of the southwestern desert of Egypt. Ann. Geol. Surv. Egypt 11, 57–66.

Table 1

Jerris, T., 2014. Development of structural basins and domes on the Sinn El-Kaddab Plateau, Egypt: Insights from in situ data and application of moderate resolution orbital imagery of the Seiyal fault. Master's thesis, Missouri University of Science and Technology.

Jimenez, G., 2014. Travertine from Egypt's Western Desert: a Terrestrial Record of North African paleohydrology and paleoclimate during the late Pleistocene. Master's thesis, University of New Mexico.

Khan, S.D., Mohamed S.F., Abdelazeem, M., 2014. Remote sensing and geophysical investigations of Moghra Lake in the Qattara Depression, Western Desert, Egypt. Geomorphology 207, 10–22.

Keatings, K., Tassie, G.J., Flower, R.J., Hassan, F.A., Hamdan, M.A.R., Hughes, M., Arrowsmith, C., 2007. An examination of groundwater within the Hawara Pyramid, Egypt. Geoarchaeology 22, 533–554.

Kieniewicz, J.M., Smith, J.R., 2007. Hydrologic and climatic implications of stable isotope and minor element analyses of authigenic calcite silts and gastropod shells from a mid-Pleistocene pluvial lake, Western Desert, Egypt. Quat. Res. 68, 431–444.

Kieniewicz, J.M., Smith, J.R., 2009. Paleoenvironmental reconstruction and water balance of a mid-Pleistocene pluvial lake, Dakhleh Oasis, Egypt. Geol. Soc. Am. Bull. 121, 1154–1171.

Kochel, R.G., Piper, J.F., 1986. Morphology of large valleys on Hawaii: Evidence for groundwater sapping and comparisons with Martian valleys, in: Lunar and Planetary Science Conference Proceedings. p. 175.

Kröpelin, S., 1993. Geomorphology, landscape evolution and paleoclimates of southwest Egypt. Catena Suppl. 26, 31–66.

Table 1

Kuss, J., Scheibner, C., Gietl, R., 2000. Carbonate platform to basin transition along an upper Cretaceous to lower tertiary Syrian Arc uplift, Galala Plateaus, Eastern Desert, Egypt. GeoArabia 5, 405–424.

Laity, J., 1988. The role of groundwater sapping in valley evolution on the Colorado Plateau. Sapping Featur. Color. Plateau. 63–70.

Laity, J.E., Malin, M.C., 1985. Sapping processes and the development of theater-headed valley networks on the Colorado Plateau. Geol. Soc. Am. Bull. 203–217.

Lamb, M.P., Howard, A.D., Johnson, J., Whipple, K.X., Dietrich, W.E., Perron, J.T., 2006. Can springs cut canyons into rock? J. Geophys. Res. Planets 111.

Lamb, M.P., Dietrich, W.E., Aciego, S.M., Depaolo, D.J., Manga, M., 2008. Formation of Box Canyon, Idaho, by megaflood: implications for seepage erosion on Earth and Mars. Science 320, 1067–1070. doi:10.1126/science.1156630

Lamb, M.P., Dietrich, W.E., 2009. The persistence of waterfalls in fractured rock. Geol. Soc. Am. Bull. 121, 1123–1134.

Lamb, M.P., Mackey, B.H., Farley, K.A., 2014. Amphitheater-headed canyons formed by megaflooding at Malad Gorge, Idaho. Proc. Natl. Acad. Sci. U. S. A. 111, 57–62. doi:10.1073/pnas.131225111.

Lehmann, K.K., Berden, G., Engeln, R., 2009. An introduction to cavity ringdown spectroscopy. Cavity Ringdown Spectrosc. Tech. Appl. G.Berden R.Engeln, eds. (Wiley, 2009) 1–26.

Li, C., Liu, L., Wang, J., Zhao, C., Wang, R., 2004. Comparison of two methods of the fusion of remote sensing images with fidelity of spectral information, in: Geoscience and Remote Sensing Symposium, 2004. IGARSS'04. Proceedings. 2004 IEEE International. IEEE, pp. 2561–2564.

Table 1

Luo, W., 2000. Quantifying groundwater sapping landforms with a hypsometric technique. J. Geophys. Res. Planets 105, 1685–1694.

Luo, W., Arvidson, R.E., Sultan, M., Becker, R., Crombie, M.K., Sturchio, N., El Alfy, Z., 1997. Ground-water sapping processes, Western Desert, Egypt. Geol. Soc. Am. Bull. 109, 43–62. doi:10.1130/0016-7606(1997)109<0043

Luo, W., Howard, A.D., 2008. Computer simulation of the role of groundwater seepage in forming Martian valley networks. J. Geophys. Res. Planets 113.

Malin, M.C., Edgett, K.S., 2000. Evidence for recent groundwater seepage and surface runoff on Mars. Science 288, 2330–2335. doi:8640 [pii]

Marra, W.A., Braat, L., Baar, A.W., Kleinhans, M.G., 2014. Valley formation by groundwater seepage, pressurized groundwater outbursts and crater-lake overflow in flume experiments with implications for Mars. Icarus 232, 97–117.

Marra, W.A., McLelland, S. J., Parsons, D. R., Murphy, B. J., Hauber, E., and Kleinhans, M. G., 2015. Groundwater seepage landscapes from distant and local sources in experiments and on Mars. Earth Surf. Dyn. 3, 389–408.

Martınez-Casasnovas, J.A., Ramos, M.C., Poesen, J., 2004. Assessment of sidewall erosion in large gullies using multi-temporal DEMs and logistic regression analysis. Geomorphology 58, 305–321.

Mastronuzzi, G., Sansò, P., 2002. Pleistocene sea level changes, sapping processes and development of valley networks in the Apulia region (southern Italy). Geomorphology 46, 19–34.

Maxwell, T.A., 1982. Erosional patterns of the Gilf Kebir Plateau and implications of the origin of martian Canyonlands, in El-Baz, F., and Maxwell, T. A., (eds.), Desert landforms of

Table 1

southwest Egypt; A basis for comparison with Mars: National Aeronautics and Space Adminstration CR-3611, pp. 281-300.

McCauley, J.F., Schaber, G.G., Breed, C.S., Grolier, M.J., Haynes, C.V, Issawi, B., Elachi, C., Blom, R., 1982. Subsurface valleys and geoarcheology of the eastern sahara revealed by shuttle radar. Science 218, 1004–1020. doi:218/4576/1004

McEwen, A. S., Keszthelyi, L. P. and Grant, J. A., 2012. Have there been large, recent (Mid-Late Amazonian) water floods on Mars? Lunar and Planetary Science Conference. 43, 1612.

McEwen, A.S., Dundas, C.M., Mattson, S.S., Toigo, A.D., Ojha, L., Wray, J.J., Chojnacki, M., Byrne, S., Murchie, S.L., Thomas, N., 2014. Recurring slope lineae in equatorial regions of Mars. Nature Geoscience 7, 53–58.

McLaren, S.J., Al-Juaidi, F., Bateman, M.D., Millington, A.C., 2009. First evidence for episodic flooding events in the arid interior of central Saudi Arabia over the last 60 ka. J. Quat. Sci. 24, 198–207.

Mohamed, A., Sultan, M., Ahmed, M., Eugene, Y.A., 2015. Towards a better understanding of the hydrologic setting of the Nubian Sandstone Aquifer System: Inferences from groundwater flow models, CL-36 ages, and GRACE data. AGU, San Fransisco.

Montgomery, D.R., Gillespie, A., 2005. Formation of Martian outflow channels by catastrophic dewatering of evaporite deposits. Geology 33, 625–628.

Montgomery, D.R., Som, S.M., Jackson, M.P.A., Schreiber, B.C., Gillespie, A.R., Adams, J.B., 2009. Continental-scale salt tectonics on Mars and the origin of Valles Marineris and associated outflow channels. Geol. Soc. Am. Bull. 121, 117–133.

Table 1

Moustafa, A.R., 2002. Structural style and timing of Syrian Arc deformation in northern Egypt, in: Abstracts, American Association of Petroleum Geologists, International Conference, Cairo.

Nash, D.J., 1996. Groundwater sapping and valley development in the Hackness Hills, North Yorkshire, England. Earth Surf. Process. Landforms 21, 781–795.

Neev, D., Hall, J.K., 1982. A global system of spiraling geosutures. J. Geophys. Res. Solid Earth 87, 10689–10708.

Neev, D., Hall, J.K., Saul, J.M., 1982. The Pelusium megashear system across Africa and associated lineament swarms. J. Geophys. Res. Solid Earth 87, 1015–1030.

New, M., Hulme, M., Jones, P., 2000. Representing twentieth-century space-time climate variability. Part II: Development of 1901–96 monthly grids of terrestrial surface climate. J. Clim. 13, 2217–2238.

Nicoll, K., 1998. Holocene playas as sedimentary evidence for recent climate change in the presently hyperarid Western Desert, Egypt. PhD Thesis, University of Arizona, 291 pp.

Nicoll, K., Giegengack, R., Kleindienst, M., 1999. Petrogenesis of artifact-bearing fossil spring tufa deposits from Kharga Oasis, Egypt. Geoarchaeology 14, 849–863.

O'Callaghan, J.F., Mark, D.M., 1984. The extraction of drainage networks from digital elevation data. Comput. vision, Graph. image Process. 28, 323–344.

Onda, Y., 1994. Seepage erosion and its implication to the formation of amphitheatre valley heads: a case study at Obara, Japan. Earth Surf. Process. Landforms 19, 627–640.

Pachur, H. J., Hoelzmann, P., 2000. Late Quaternary palaeoecology and palaeoclimates of the eastern Sahara. J. African Earth Sci. 30, 929–939.

Table 1

Paillou, P., Grandjean, G., Baghdadi, N., Heggy, E., August-Bernex, T., Achache, J., 2003. Subsurface imaging in south-central Egypt using low-frequency radar: bir safsaf revisited. IEEE Trans. Geosci. Remote Sens. 41, 1672–1684. doi:10.1109/TGRS.2003.813275

Paillou, P., Bernard, D., Radebaugh, J., Lorenz, R., Le Gall, A., Farr, T., 2014. Modeling the SAR backscatter of linear dunes on Earth and Titan. Icarus 230, 208–214.

Patterson, L.J., Sturchio, N.C., Kennedy, B.M., van Soest, M.C., Sultan, M., Lu, Z., Lehmann, B., Purtschert, R., El Alfy, Z., El Kaliouby, B., 2005. Cosmogenic, radiogenic, and stable isotopic constraints on groundwater residence time in the Nubian Aquifer, Western Desert of Egypt. Geochemistry, Geophys. Geosystems 6.1-19.

Pederson, D.T., 2001. Stream piracy revisited: A groundwater-sapping solution. GSA Today 11, 4-11.

Pedrera, A., Pérez-Peña, J.V., Galindo-Zaldívar, J., Azañón, J.M., Azor, A., 2009. Testing the sensitivity of geomorphic indices in areas of low-rate active folding (eastern Betic Cordillera, Spain). Geomorphology 105, 218–231.

Pelletier, J.D., Baker, V.R., 2011. The role of weathering in the formation of bedrock valleys on Earth and Mars: A numerical modeling investigation. J. Geophys. Res. Planets 116.

Rayan, A., Fernandes, R.M.S., Khalil, H.A., Mahmoud, S., Miranda, J.M., Tealab, A., 2010. Evaluation of the crustal deformations in the northern region of Lake Nasser (Egypt) derived from 8 years of GPS campaign observations. J. Geodyn. 49, 210–215.

REGWA, 1990. Hydrogeological inventory and groundwater development plan, western Nile Delta Region. Internal report.

Table 1

RIGW, 1992. Groundwater resources and projection of groundwater development, Water Security Project. National Water Research Center, Egypt, 37 pp.

Robinson, C.A., 2002. Application of satellite radar data suggest that the Kharga Depression in south-western Egypt is a fracture rock aquifer. Int. J. Remote Sens. 23, 4101–4113.

Rossi, A.P., Neukum, G., Pondrelli, M., van Gasselt, S., Zegers, T., Hauber, E., Chicarro, A., Foing, B., 2008. Large-scale spring deposits on Mars? J. Geophys. Res. Planets 113.

Said, R., 1962. The geology of Egypt. Elseveir, Amsterdam.

Said, R., 1979. The Messinian in Egypt. Proc.Intern.Congr.Mediterranean Neogene, Athens.Ann.Geol.Pays Hell. Hors Ser., Fasc 101, 1083–1090.

Said, R., 1983. Proposed classification of the Quaternary of Egypt. J. African Earth Sci. 1, 41–45.

Saleh, S., 2011. Subsurface structural mapping of Northern Nasser Lake region, Aswan, Egypt, using Bouguer data. Contrib. to Geophys. Geod. 41, 45–72.

Salem, O., Pallas, P., 2004. The Nubian Sandstone Aquifer System (NSAS). In: Appelgren B (ed) Managing shared aquifer resources in Africa. ISARM-Africa. IHP-VI, Series on Groundwater no. 8, UNESCO, Paris, 19–22.

Salman, A.B., Howari, F.M., El-Sankary, M.M., Wali, A.M., Saleh, M.M., 2010. Environmental impact and natural hazards on Kharga Oasis monumental sites, Western Desert of Egypt. J. African Earth Sci. 58, 341–353.

Sanz-Montero, M.E., Wanas, H., Muñoz-García, M.B., González-Acebrón, L., López, M. V, 2013. The uppermost deposits of the stratigraphic succession of the Farafra Depression (Western Desert, Egypt): Evolution to a Post-Eocene continental event. J. African Earth Sci. 87, 33–43.

Table 1

Schaber, G.G., McCauley, J.F., Breed, C.S., 1997. The use of multifrequency and polarimetric SIR-C/X-SAR data in geologic studies of Bir Safsaf, Egypt. Remote Sens. Environ. 59, 337–363.

Schumm, S.A., Boyd, K.F., Wolff, C.G., Spitz, W.J., 1995. A ground-water sapping landscape in the Florida Panhandle. Geomorphology 12, 281–297.

Schumm, S.A., Phillips, L., 1986. Composite channels of the Canterbury Plain, New Zealand: A martian analog? Geology 14, 326–329.

Shata, A.A., 1982. Hydrogeology of the great Nubian Sandstone basin, Egypt. Q. J. Eng. Geol. Hydrogeol. 15, 127–133.

Simpkins, W.W., and Baumgardner, R.W., 1982. Stream incision and scarp retreat rates based on volcanic ash date from the Seymour Formation, in: Gustavson, T.C. (Eds.), Geology and Geohydrology of the Palo Duro Basin, Texas Panhandle—A Report on the Progress of Nuclear Waste Isolation Feasibility Studies (1981). University of Texas at Austin, Bureau of Economic Geology, Austin, 160–163.

Smith, B.J., 2009. Weathering processes and forms, in: Geomorphology of Desert Environments. Springer, 69–100.

Smith, J.R., 2001. Geoarchaeology, stable-isotope geochemistry, and geochronology of fossil-spring tufas, Western Desert, Egypt. PhD Thesis, University of Pennsylvania, Philadelphia, 180 pp.

Smith, J.R., Giegengack, R., Schwarcz, H.P., 2004a. Constraints on Pleistocene pluvial climates through stable-isotope analysis of fossil-spring tufas and associated gastropods, Kharga Oasis, Egypt. Palaeogeogr. Palaeoclimatol. Palaeoecol. 206, 157–175.

Table 1

Smith, J.R., Giegengack, R., Schwarcz, H.P., McDonald, M.M., Kleindienst, M.R., Hawkins, A.L., Churcher, C.S., 2004b. A reconstruction of Quaternary pluvial environments and human occupations using stratigraphy and geochronology of fossil-spring tufas, Kharga Oasis, Egypt. Geoarchaeology 19, 407–439. doi:10.1002/gea.20004

Sonntag, C., Muennich, K.O., Junghans, C., Klitzsch, E., Thorweihe, U., Weistroffer, K., Loehnert, E.P., Swailem, F.M., 1978. Paleoclimatic information from deuterium and oxygen-18 in C-14 dated north Saharian groundwaters. In: Isotope Hydrology, 978. International Atomic Energy Agency, Vienna, 569–580.

Squyres, C.H., Bradley, W., 1964. Notes on the Western Desert of Egypt, in: Conference Petroleum Exploration Society, Libya. 99–105.

Stern, R.J., 1985. The Najd Fault System, Saudi Arabia and Egypt: A Late Precambrian rift-related transform system? Tectonics 4, 497–511.

Stöckl, L., 2010. Hydrological and hydrochemical controls on radioactivity in deep groundwater in Saudi Arabia. Master Thesis, Albert-Luwigs Universitat Freiburg. 79 pp.

Stuiver, M., Polach, H.A., 1977. Discussion; reporting of C-14 data. Radiocarbon 19, 355–363.

Sturchio, N.C., Arehart, G.B., Sultan, M., Sano, Y., AboKamar, Y., Sayed, M., 1996. Composition and origin of thermal waters in the Gulf of Suez area, Egypt. Appl. Geochemistry 11, 471–479.

Sturchio, N.C., Du, X., Purtschert, R., Lehmann, B.E., Sultan, M., Patterson, L.J., Lu, Z., Müller, P., Bigler, T., Bailey, K., 2004. One million year old groundwater in the Sahara revealed by krypton-81 and chlorine-36. Geophys. Res. Lett. 31.

Table 1

Sultan, M., Arvidson, R.E., Duncan, I.J., Stern, R.J., El Kaliouby, B., 1988. Extension of the Najd shear system from Saudi Arabia to the central Eastern Desert of Egypt based on integrated field and Landsat observations. Tectonics 7, 1291–1306.

Sultan, M., Becker, R., Arvidson, R.E., Shore, P., Stern, R.J., El Alfy, Z., Attia, R.I., 1993. New constraints on Red Sea rifting from correlations of Arabian and Nubian Neoproterozoic outcrops. Tectonics 12, 1303–1319.

Sultan, M., Sturchio, N., Hassan, F.A., Hamdan, M.A.R., Mahmood, A.M., El Alfy, Z., Stein, T., 1997. Precipitation source inferred from stable isotopic composition of Pleistocene groundwater and carbonate deposits in the Western desert of Egypt. Quat. Res. 48, 29–37.

Sultan, M., Sturchio, N.C., Gheith, H., Hady, Y.A., Anbeawy, M., 2000. Chemical and Isotopic Constraints on the Origin of Wadi El-Tarfa Ground Water, Eastern Desert, Egypt. Groundwater 38, 743–751.

Sultan, M., Yan, E., Sturchio, N., Wagdy, A., Gelil, K.A., Becker, R., Manocha, N., Milewski, A., 2007. Natural discharge: a key to sustainable utilization of fossil groundwater. J. Hydrol. 335, 25–36.

Sultan, M., Yousef, A.F., Metwally, S.E., Becker, R., Milewski, A., Sauck, W., Sturchio, N.C., Mohamed, A.M.M., Wagdy, A., El Alfy, Z., 2011. Red Sea rifting controls on aquifer distribution: Constraints from geochemical, geophysical, and remote sensing data. Geol. Soc. Am. Bull. 123, 911–924.

Sultan, M., Emil, M., Abotalib, Z.A., Abouelmagd, A., Alzahrani, A., Refai, A., AlQthamy, Kh., Alaamry, M., Bahamil, A.M., 2015. Nature and timing of the Quaternary wet climatic

Table 1

periods in North Africa and Arabia: isotopic, chronologic, and remote sensing constraints. GSA abstract with programs.

Swezey, C.S., 1996. Structural controls on Quaternary depocentres within the Chotts Trough region of southern Tunisia. J. African Earth Sci. 22, 335–347.

Szabo, B.J., Haynes, C.V, Maxwell, T.A., 1995. Ages of Quaternary pluvial episodes determined by uranium-series and radiocarbon dating of lacustrine deposits of Eastern Sahara. Palaeogeogr. Palaeoclimatol. Palaeoecol. 113, 227–242.

Tarboton, D.G., 1997. A new method for the determination of flow directions and upslope areas in grid digital elevation models. Water Resour. Res. 33, 309–319.

Teng, J., Vaze, J., Tuteja, N.K., Gallant, J.C., 2008. A GIS-Based Tool for Spatial and Distributed Hydrological Modelling: CLASS Spatial Analyst. Trans. GIS 12, 209–225.

Tewksbury, B.J., Hogan, J.P., Kattenhorn, S.A., Mehrtens, C.J., Tarabees, E.A., 2014. Polygonal faults in chalk: Insights from extensive exposures of the Khoman Formation, Western Desert, Egypt. Geology 42, 479–482.

Thompson, A., 2007. Water resources of the Al Fayoum area, Egypt. Master Thesis, University of Illinois at Chicago, 43 pp.

Thorweihe, U., 1990. Nubian aquifer system. Geol. Egypt 601–614.

Thorweihe, U., Heinl, M., 2002. Groundwater resources of the Nubian aquifer system. Aquifers major basins–non-renewable water Resour. Modif. Synth.

Thurmond, A.K., Stern, R.J., Abdelsalam, M.G., Nielsen, K.C., Abdeen, M.M., Hinz, E., 2004. The Nubian Swell. J. African Earth Sci. 39, 401–407.

Table 1

Torab, M. 2013. Geomorphology of fossil springs mounds in some selected portions of Western Desert oases of Egypt, The 2nd Intl Symposium on Kaz Mountains (Mt. Ida) and Edremit (Edremit-Balikesir.

Treiman, A.H., 2008. Ancient groundwater flow in the Valles Marineris on Mars inferred from fault trace ridges. Nat. Geosci. 1, 181–183.

Vogel, J.S., Southon, J.R., Nelson, D.E., Brown, T.A., 1984. Performance of catalytically condensed carbon for use in accelerator mass spectrometry. Nucl. Instruments Methods Phys. Res. Sect. B Beam Interact. with Mater. Atoms 5, 289–293.

Wanas, H.A., 2012. Pseudospherulitic fibrous calcite from the Quaternary shallow lacustrine carbonates of the Farafra Oasis, Western Desert, Egypt: A primary precipitate with possible bacterial influence. J. African Earth Sci. 65, 105–114.

Wendorf, F., Schild, R., 1980. Prehistory of the eastern Sahara. Academic Press.

Wendorf, F., Schild, R., Close, A.E., 1984. Cattle-keepers of the eastern Sahara: the neolithic of Bir Kiseiba. Department of Anthropology [and] Institute for the Study of Earth and Man, Southern Methodist University.

Wescott, W.A., Atta, M., Blanchard, D.C., Cole, R.M., Georgeson, S.T., Miller, D.A., O'Hayer, W.W., Wilson, A.D., Dolson, J.C., Sehim, A., 2011. Jurassic Rift Architecture in the Northeastern Western Desert, Egypt. AAPG Search and Discovery Article #10379, from poster presentation at AAPG International Conference and Exhibition, Milan, Italy.

Wood, W.W., 2002. Role of ground water in geomorphology, geology, and paleoclimate of the Southern High Plains, USA. Groundwater 40, 438–447.

Table 1

Wüst, R.A.J., Schlüchter, C., 2000. The origin of soluble salts in rocks of the Thebes mountains, Egypt: The damage potential to ancient Egyptian wall art. J. Archaeol. Sci. 27, 1161–1172.

Yan, Z., Petit-Maire, N., 1994. The last 140 ka in the Afro-Asian arid/semi-arid transitional zone. Palaeogeogr. Palaeoclimatol. Palaeoecol. 110, 217–233.

Yang, X., Scuderi, L.A., Wang, X., Scuderi, L.J., Zhang, D., Li, H., Forman, S., Xu, Q., Wang, R., Huang, W., Yang, S., 2015. Groundwater sapping as the cause of irreversible desertification of Hunshandake Sandy Lands, Inner Mongolia, northern China. Proc. Natl. Acad. Sci. USA. 112, 702–706.

Table 1

TABLES

Well No.	Name	Latitude N	Longitude E	Aquifer type	DWT* (m)	δ D (‰)	δ ^{18}O (‰)
31	El-Sedk Farm	30.5137	30.0240	Production well in Pliocene	26	-12.6	-1.37
32	Sabry Harfoush Farm	30.4187	29.9163	Production well in Miocene	150	10.1	1.29
33	El-Zoghbi Farm	30.4518	29.9566	Production well in Miocene		2.6	0.42
34	Ali Salem Farm	30.4707	30.2795	Production well in Pliocene		-7.0	-1.28
36	El-Tyseer Farm	30.5782	29.8966	Production well in Pliocene		7.3	0.99
37	Abu Gamous Farm	30.5355	30.0260	Production well in Pliocene		-5.6	-0.59
38	Spring	30.3950	30.3300	Artesian spring in Pliocene	artesian	-8.6	-1.61
61	Ahmed Atyia Farm	30.2866	30.189	Production well in Miocene	190	-14.4	-2.34
62	El-Wadi Farm	30.1867	30.1047	Production well in Miocene		-15.1	-2.37
63	Bir El-Geles	28.3538	28.8653	Production well tapping Nubian	30	-81.5	-10.74
64	Bir Haddad	28.3544	28.8709	Production well tapping Nubian	8	-80.6	-10.28
65	Ain Madi well	28.3284	28.7943	Production well tapping Nubian	20	-80	-10.25
66	Bir Tamania	28.3457	28.822	Production well tapping Nubian		-83.6	-10.87
67	Bir El-Meftella	28.3593	28.8472	Production well tapping Nubian	45	-83.1	-10.83
68	Bir Walid	28.3448	28.8516	Production well tapping Nubian		-83.4	-10.79
69	Bir Segam	28.343	28.9521	Production well tapping Nubian		-83.4	-10.85
70	Ain Youssef	28.3357	29.0836	Artesian well in the Nubian	artesian	-83.7	-10.82
71	Iron Mines	28.4817	29.1824	Production well tapping Nubian	110	-84.4	-10.81
72	El-Bohour Well	28.8062	29.1602	Artesian well tapping Nubian	artesian	-83.8	-10.96

Table 1. Sample locations, well information, O and H isotopic compositions for groundwater samples from wells tapping the NAS, Miocene, and Pliocene aquifers in north Western Desert, Egypt.

Table 2

Well No.	GGAMS#	$\delta^{13}C$ (‰)	^{14}C pMC	^{14}C model age Years B.P.
31	13317	−8.8	32.81 ± 0.11	8950 ± 30
33	13318	−7.6	10.46 ± 0.06	18140 ±40
61	13319	−9.1	38.04 ± 0.13	7760 ± 30
62	13320	−8.9	35.92 ± 0.13	8230 ± 30

Table 2. Carbon isotopic data and ^{14}C model ages for investigated groundwater samples

Valley name	Minimum eroded volume	Contributing area	Notes
Box Canyon	1.46×10^7 m^3	228 km^2	Lamb et al., 2008
Blind Canyon	9.2 x10^6 m^3	4713 km^2	Lamb et al., 2008
Qattara valley (a)	151×10^7 m^3	7.03 km^2	
Qattara valley (b)	225×10^7 m^3	8.73 km^2	
Farafra valley (a)	29.6×10^7 m^3	4.92 km^2	
Farafra valley (b)	2.8×10^7 m^3	4.21 km^2	
Kharga valley (a)	61.6×10^7 m^3	13.89 km^2	
Kharga valley (b)	164×10^7 m^3	43.2 km^2	
Dakhla valley (a)	259×10^7 m^3	10.57 km^2	
Dakhla valley (b)	20.7×10^7 m^3	4.62 km^2	

Table 3. Upslope contributing areas and minimum eroded volume of selected THVs in the Sahara and in the Snake River Plain, Idaho, USA.

Figure 1

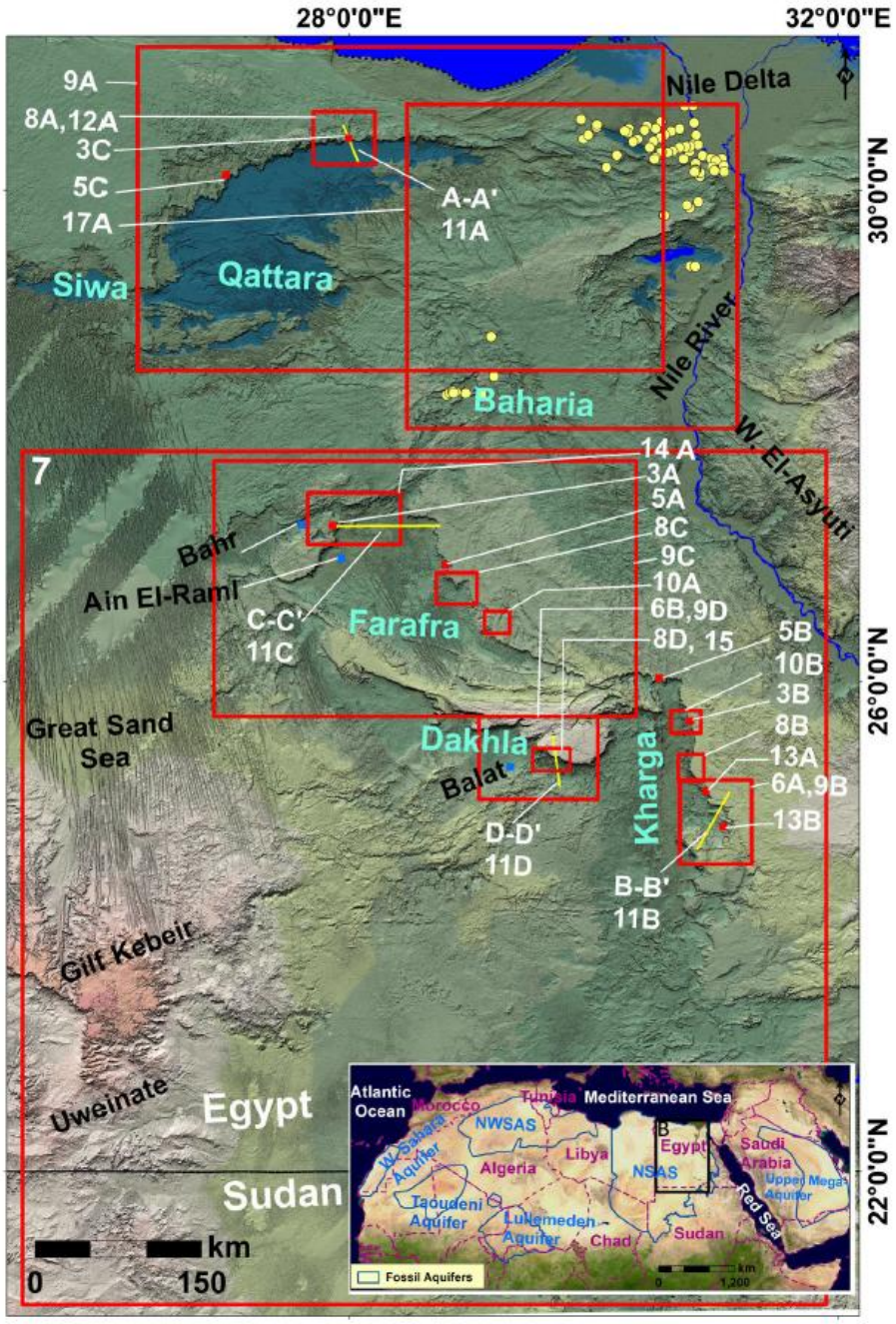

Figure 2

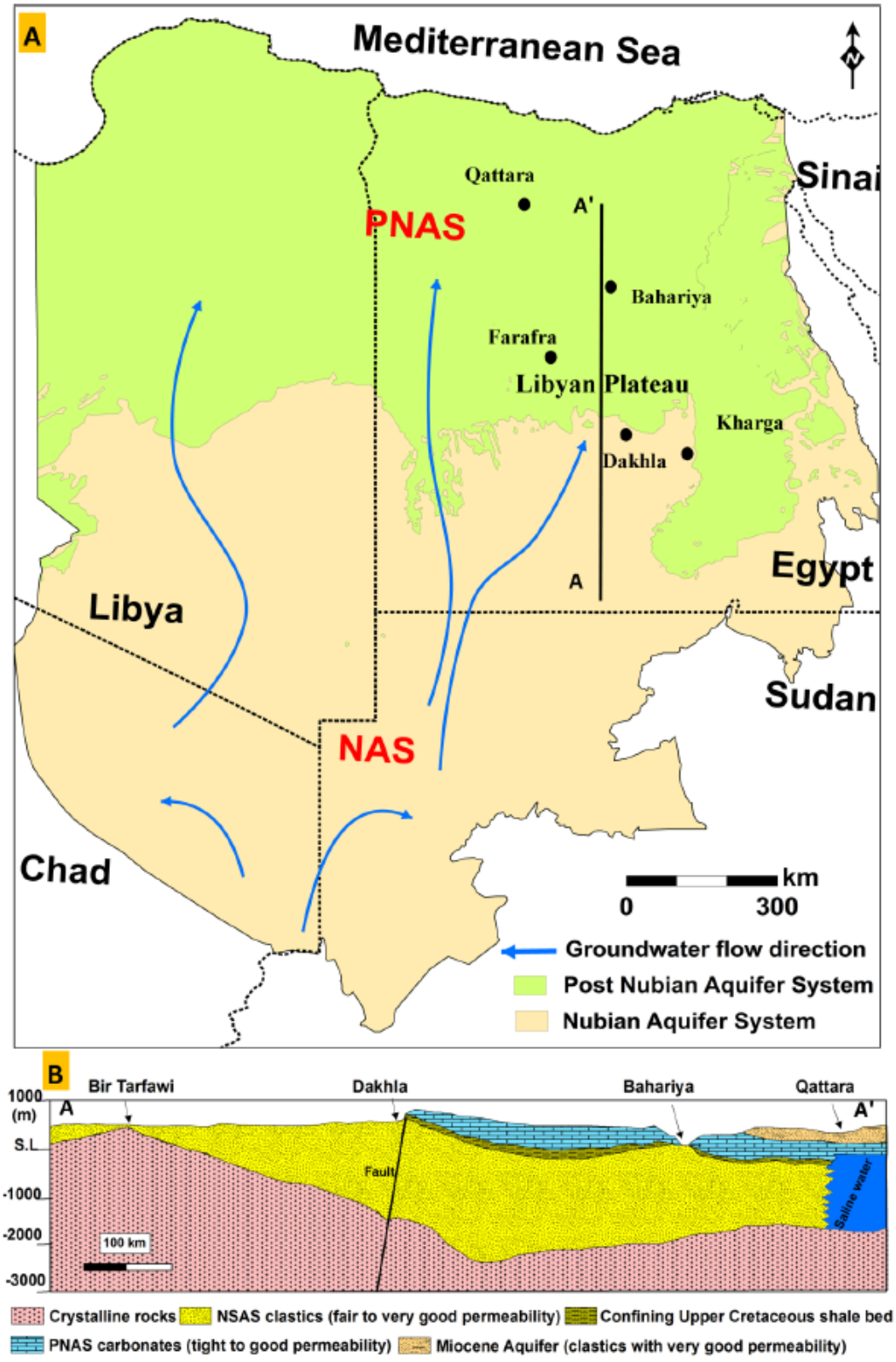

Figure 3

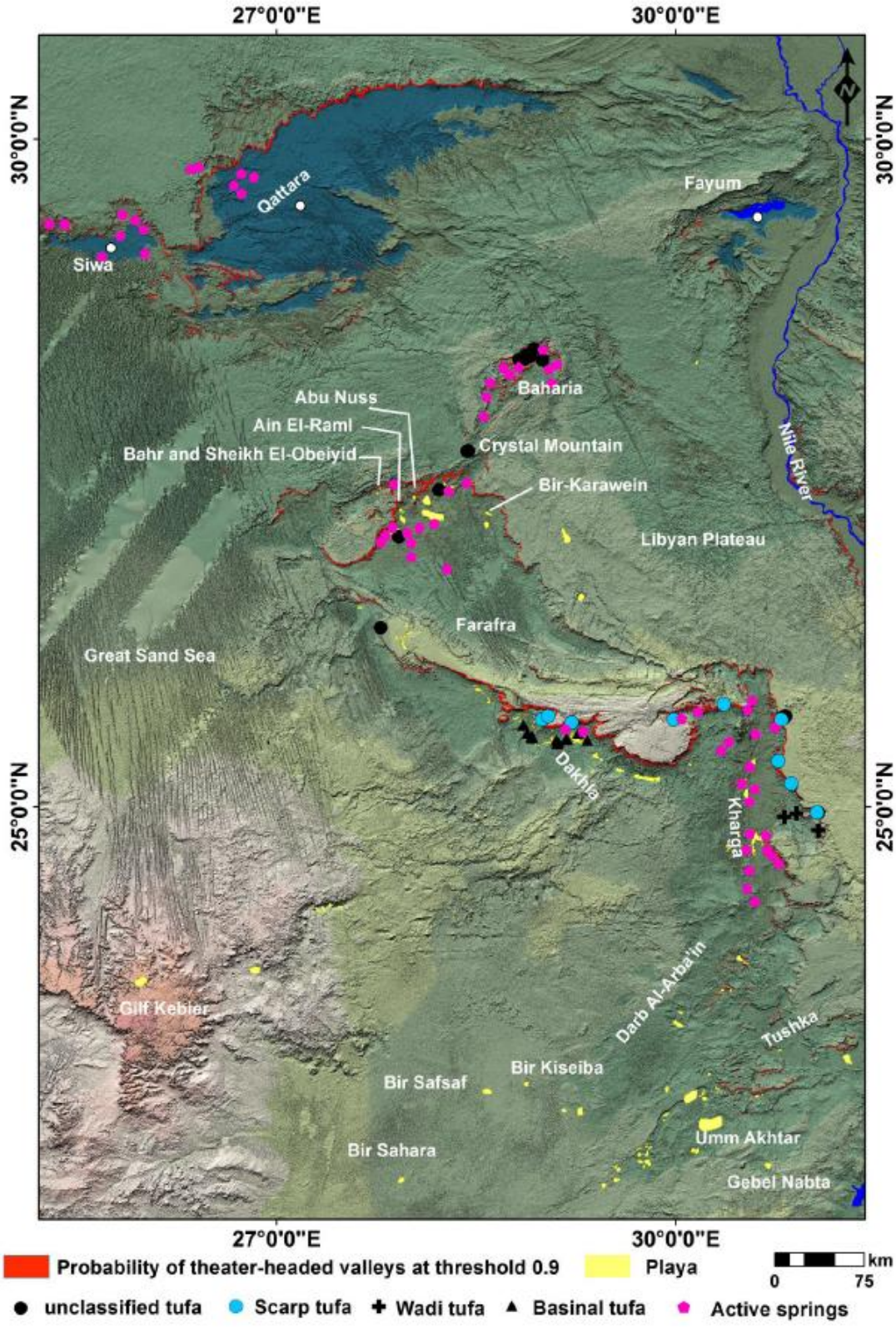

Figure 4

Figure 4

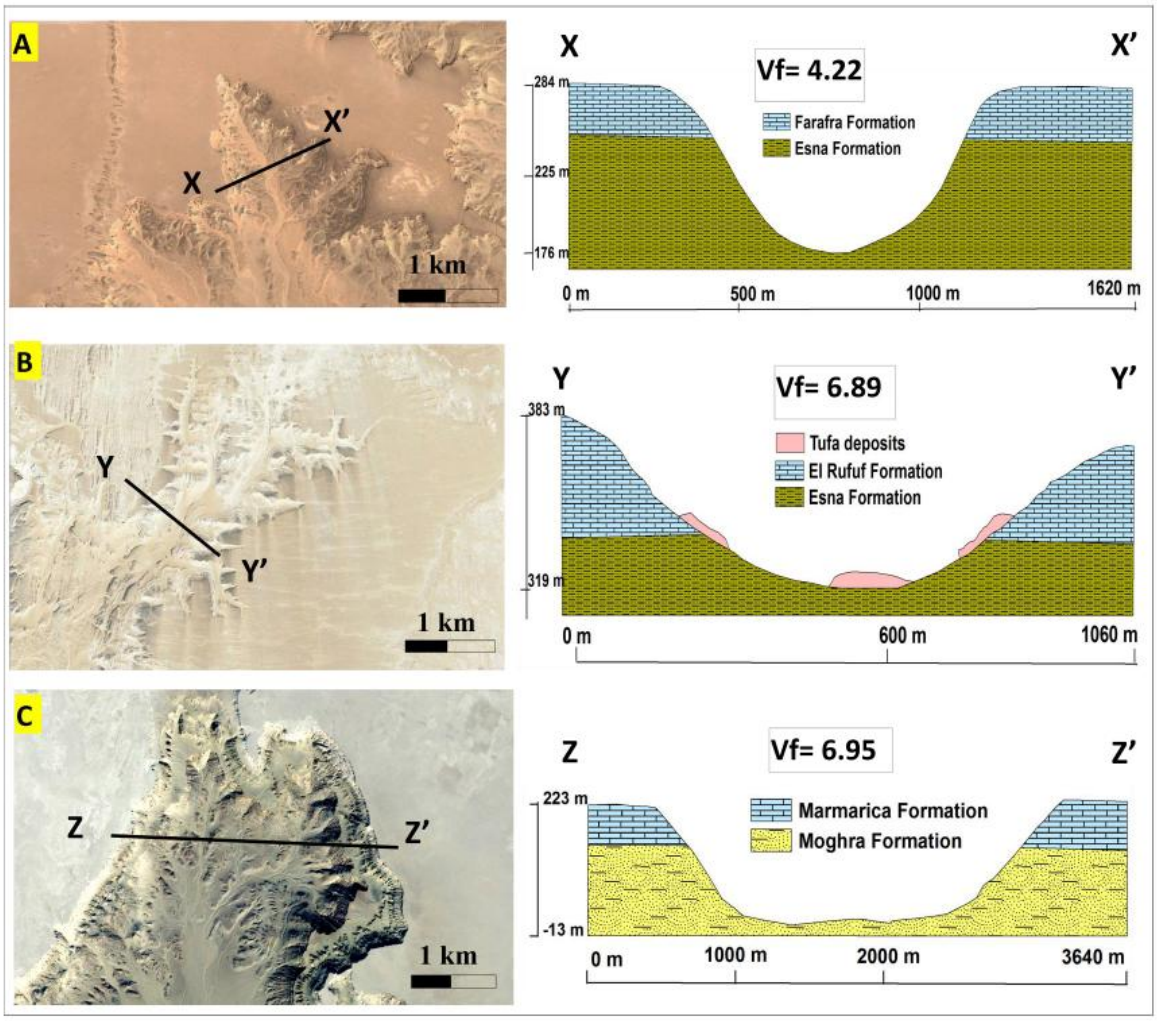

Figure 5

Figure 5

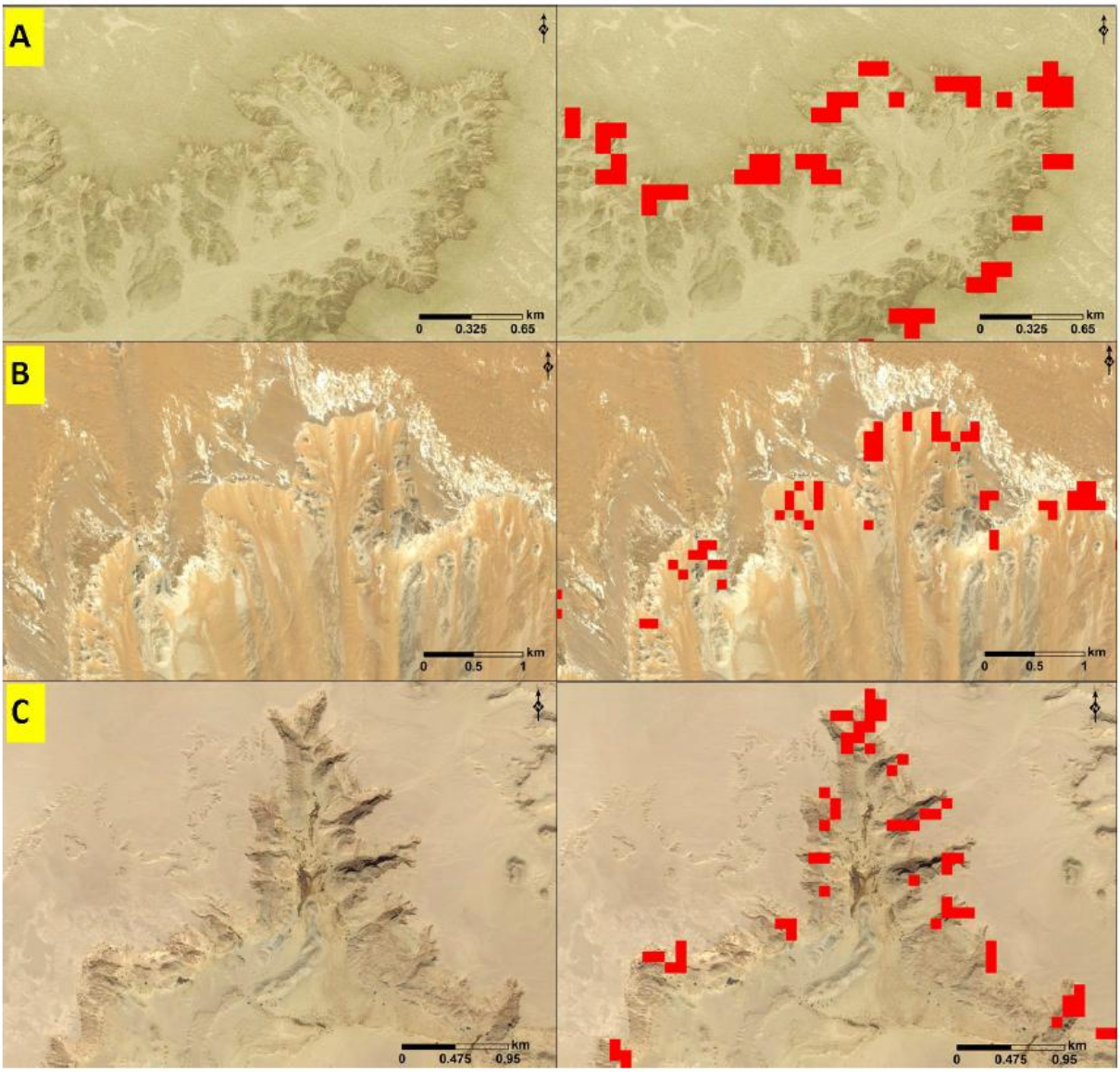

Figure 6

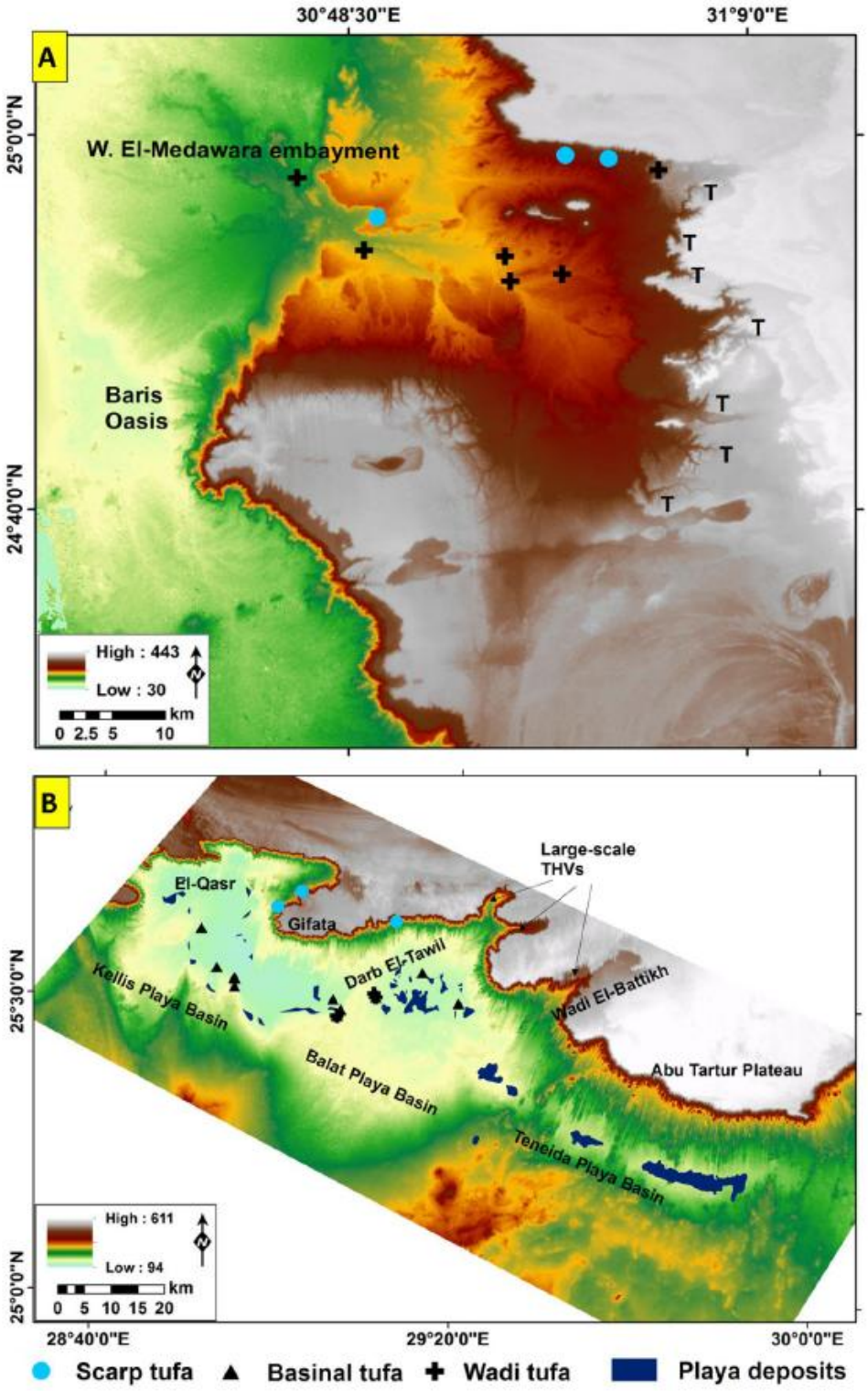

Figure 7

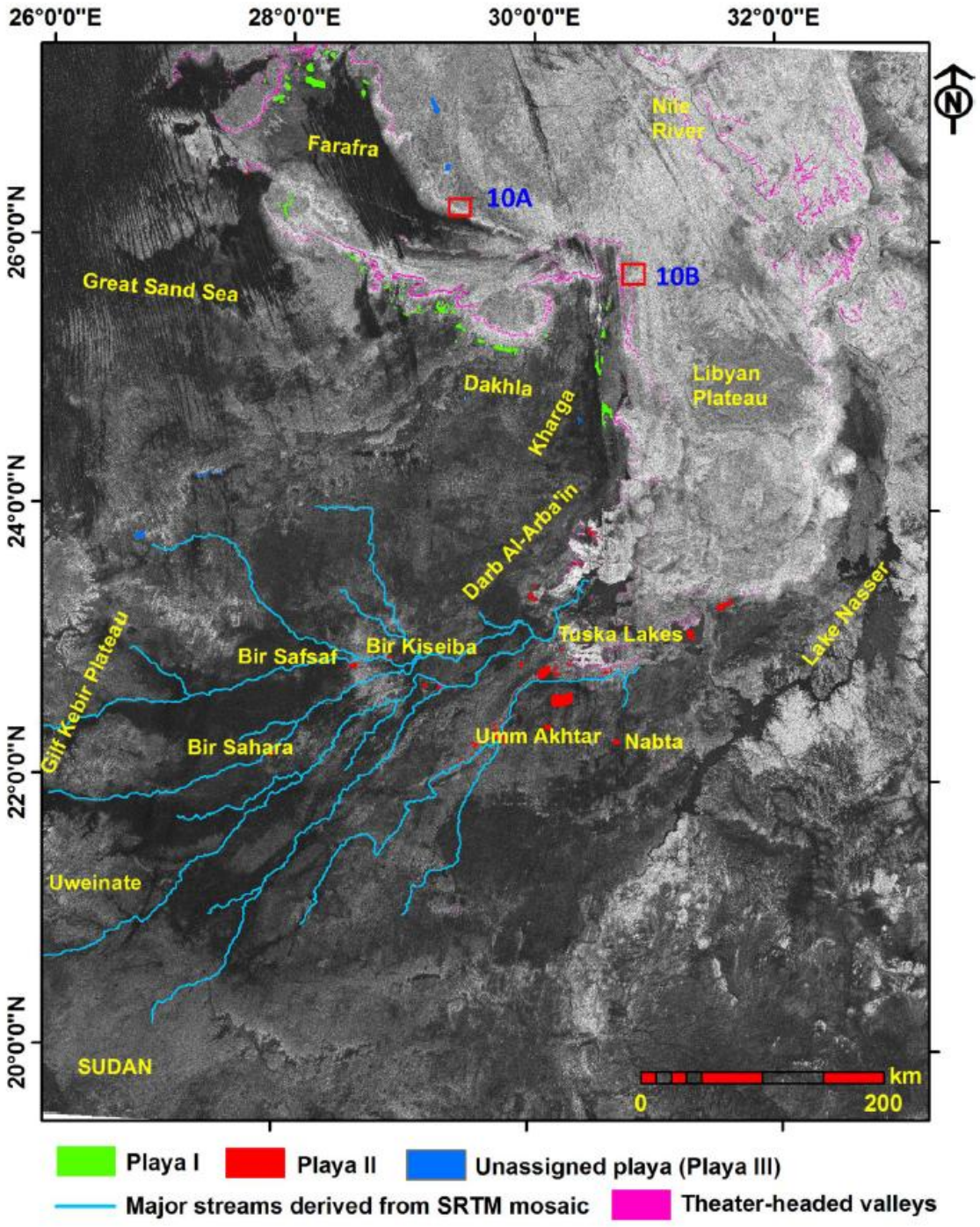

Figure 8

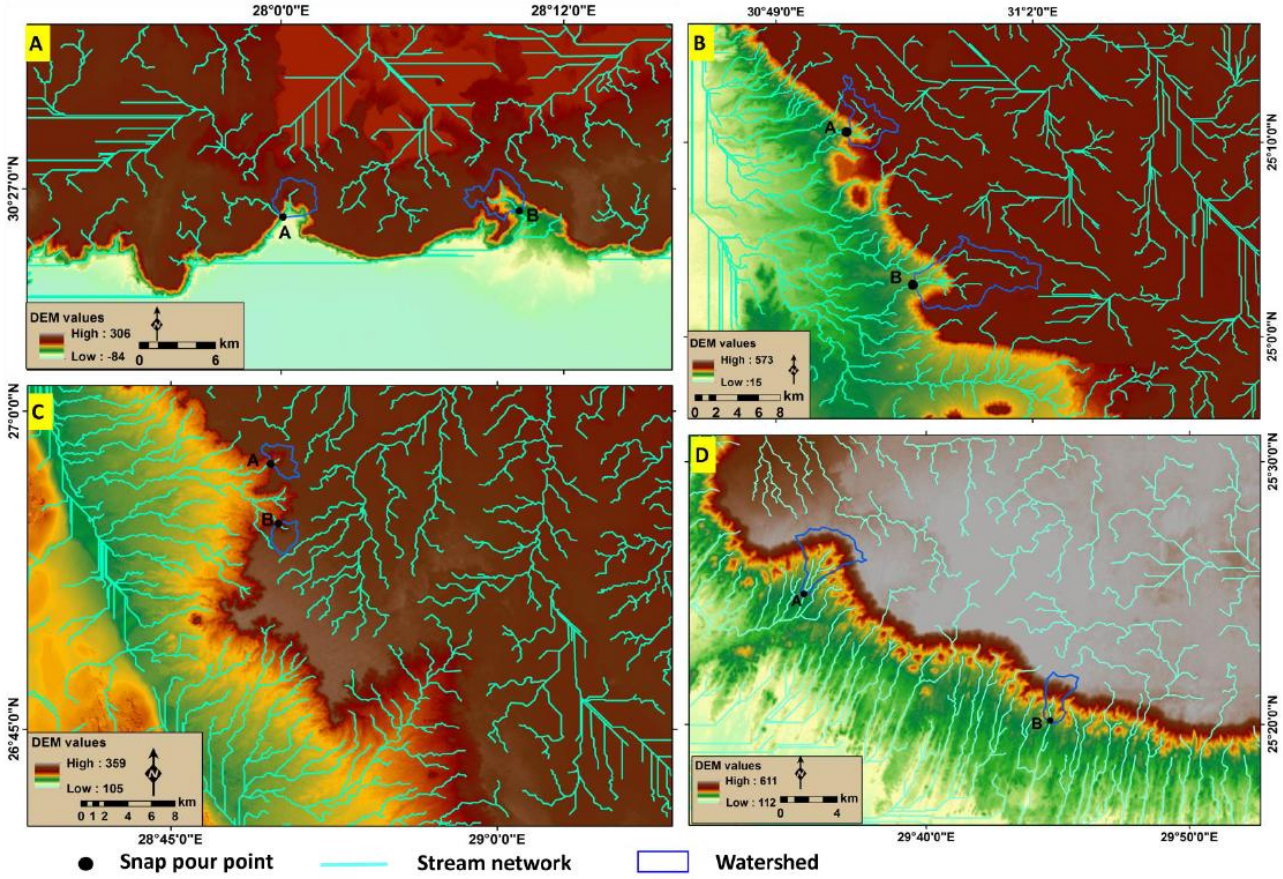

Figure 9

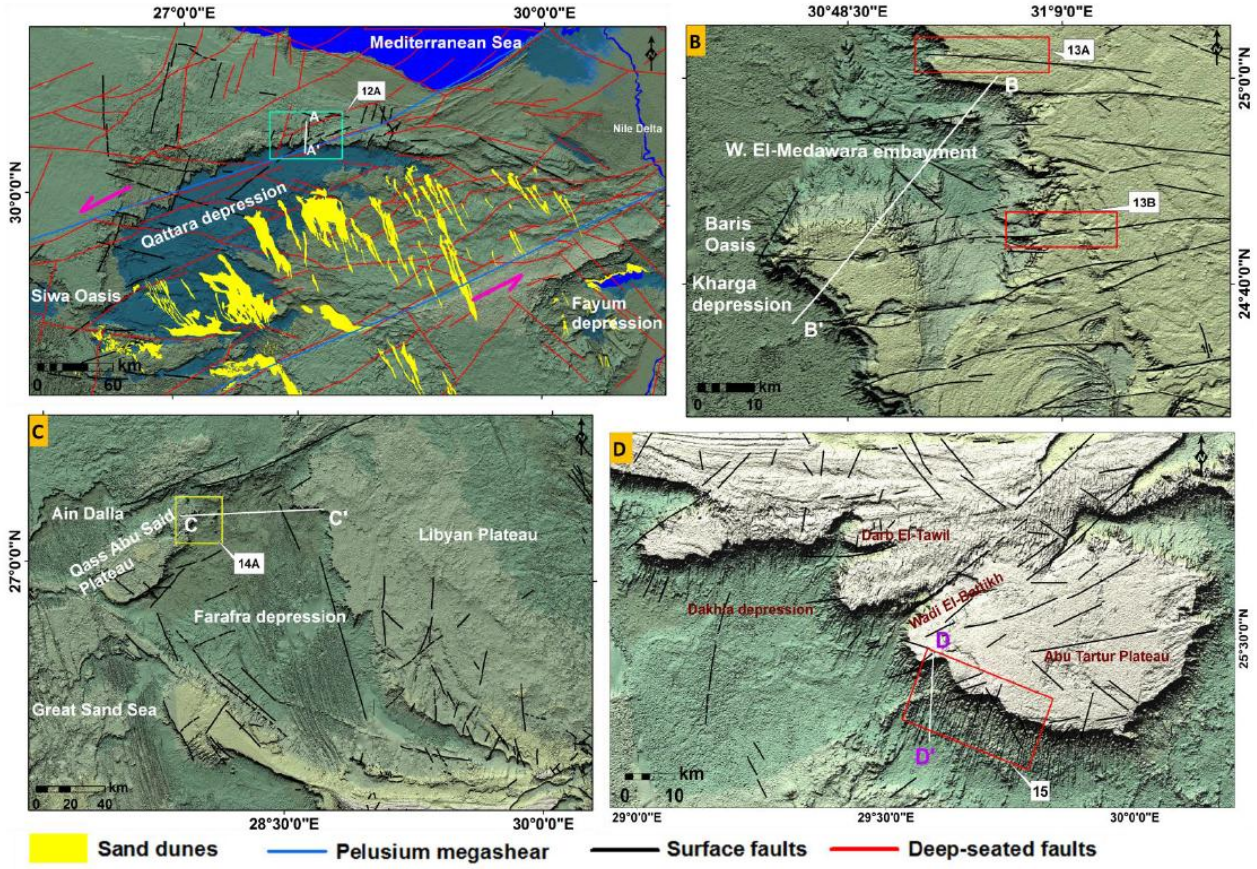

Figure 10

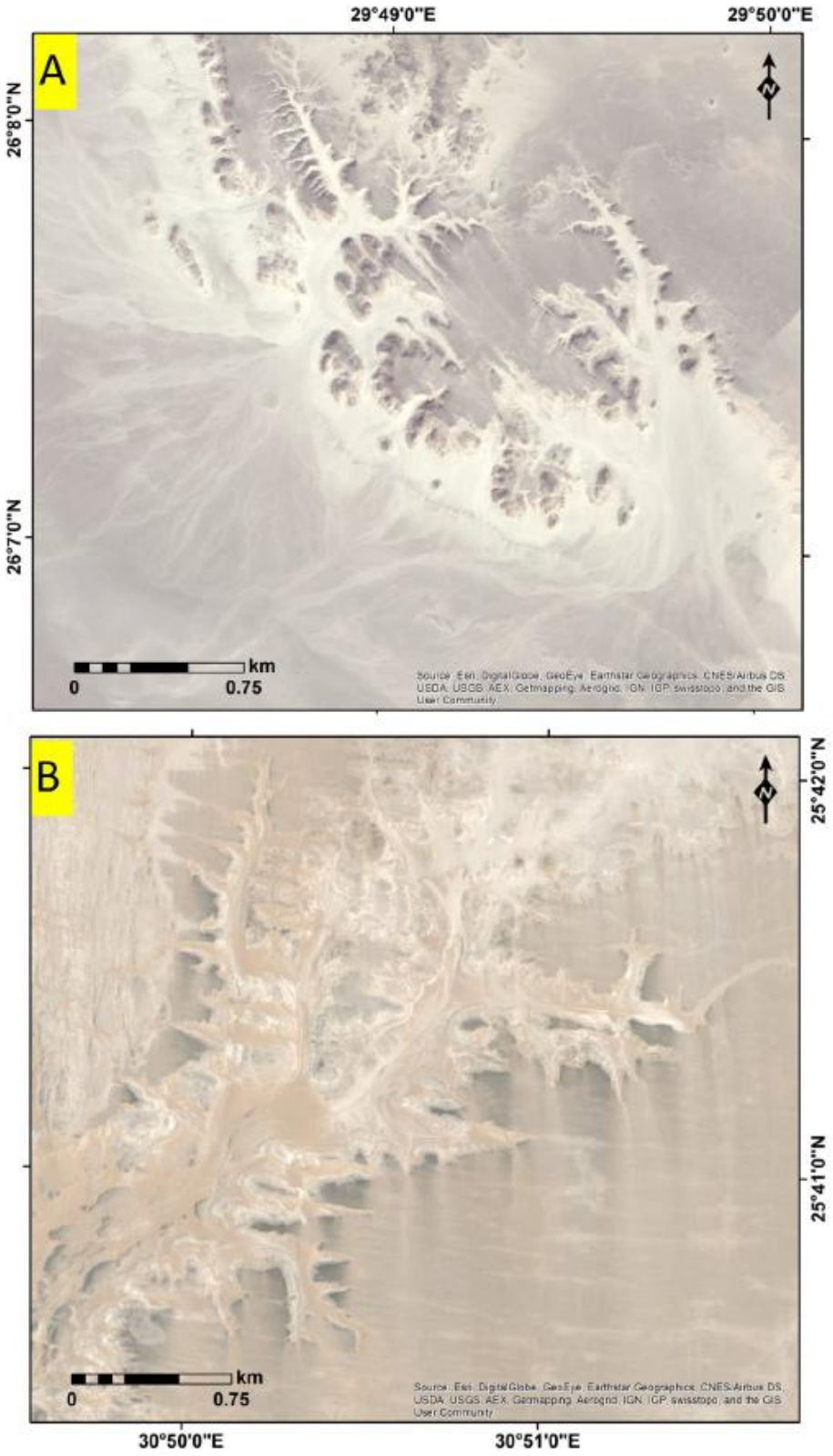

Figure 11

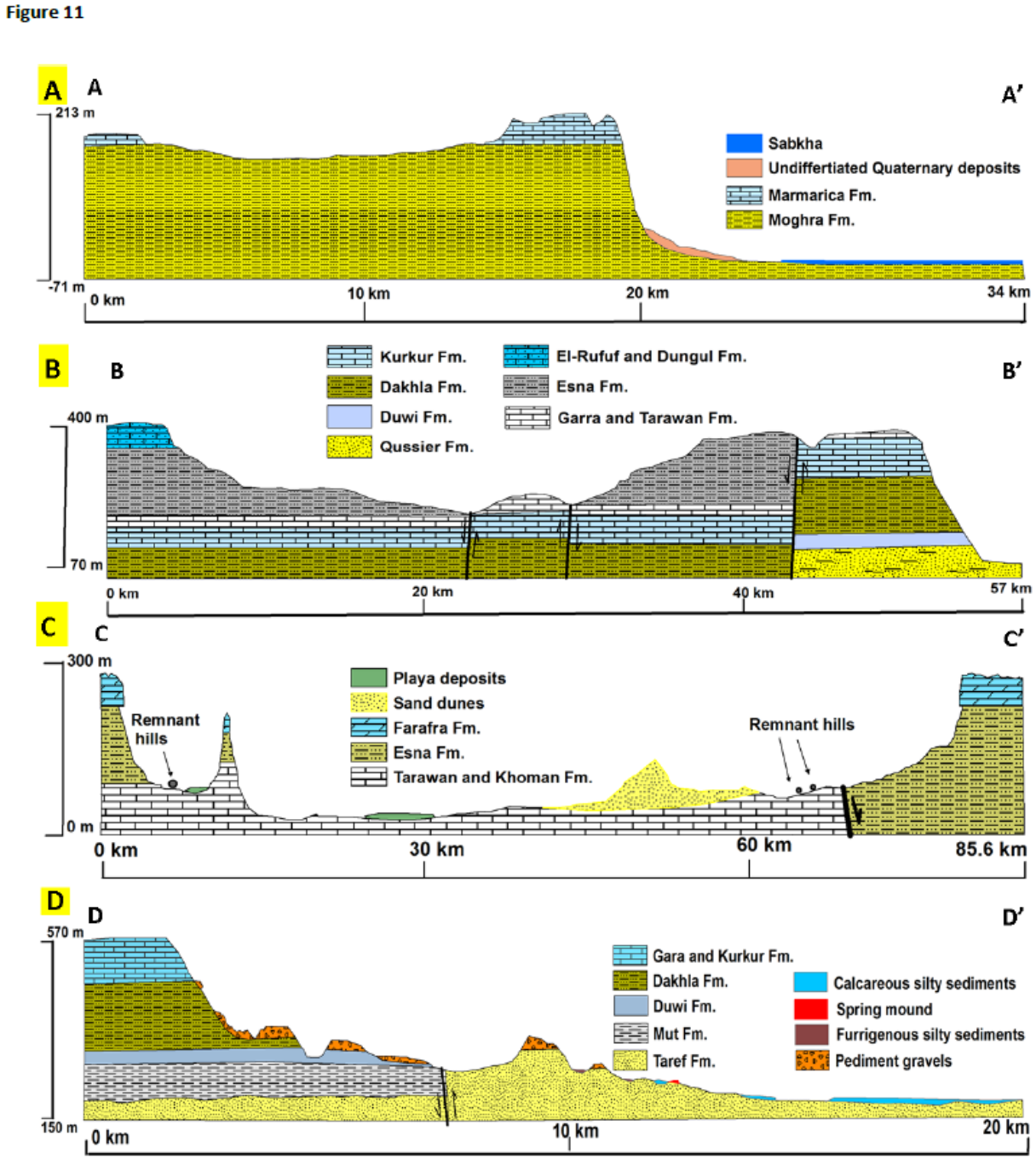

Figure 12

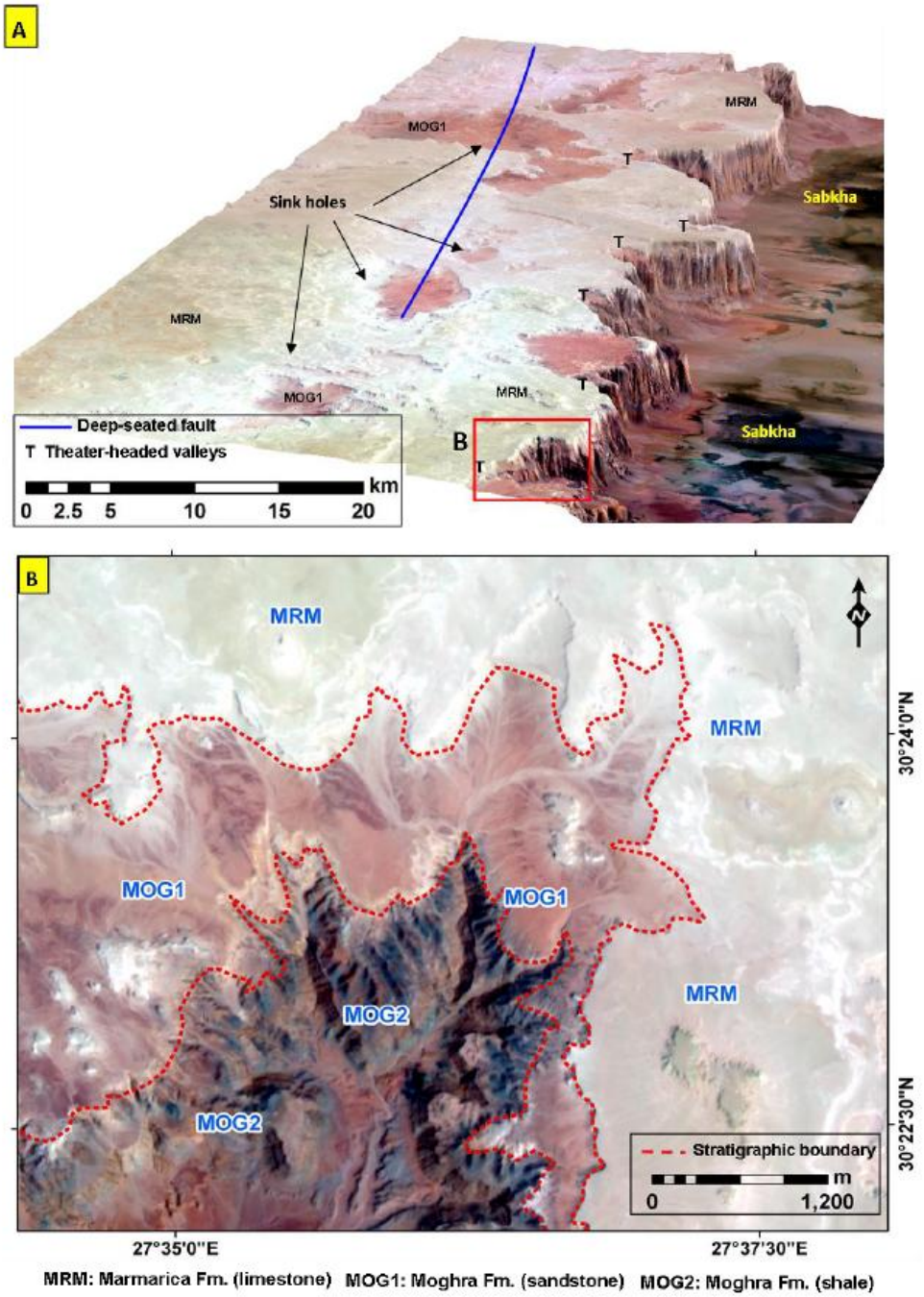

Figure 13

Figure 13

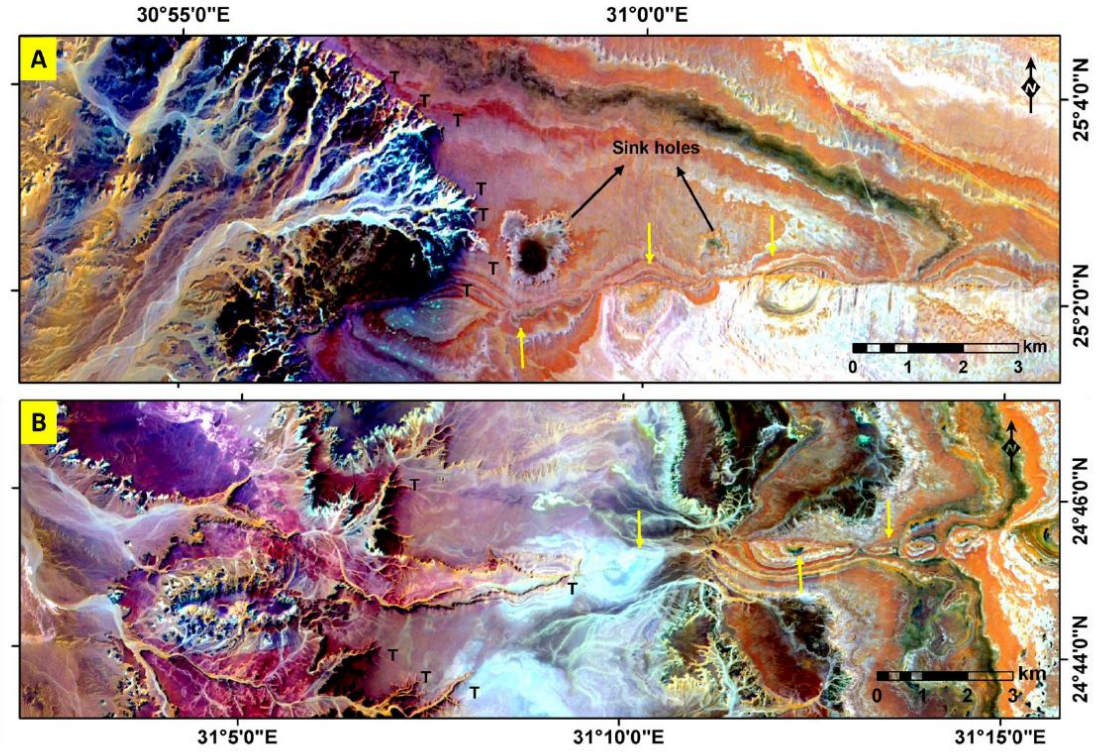

Figure 14

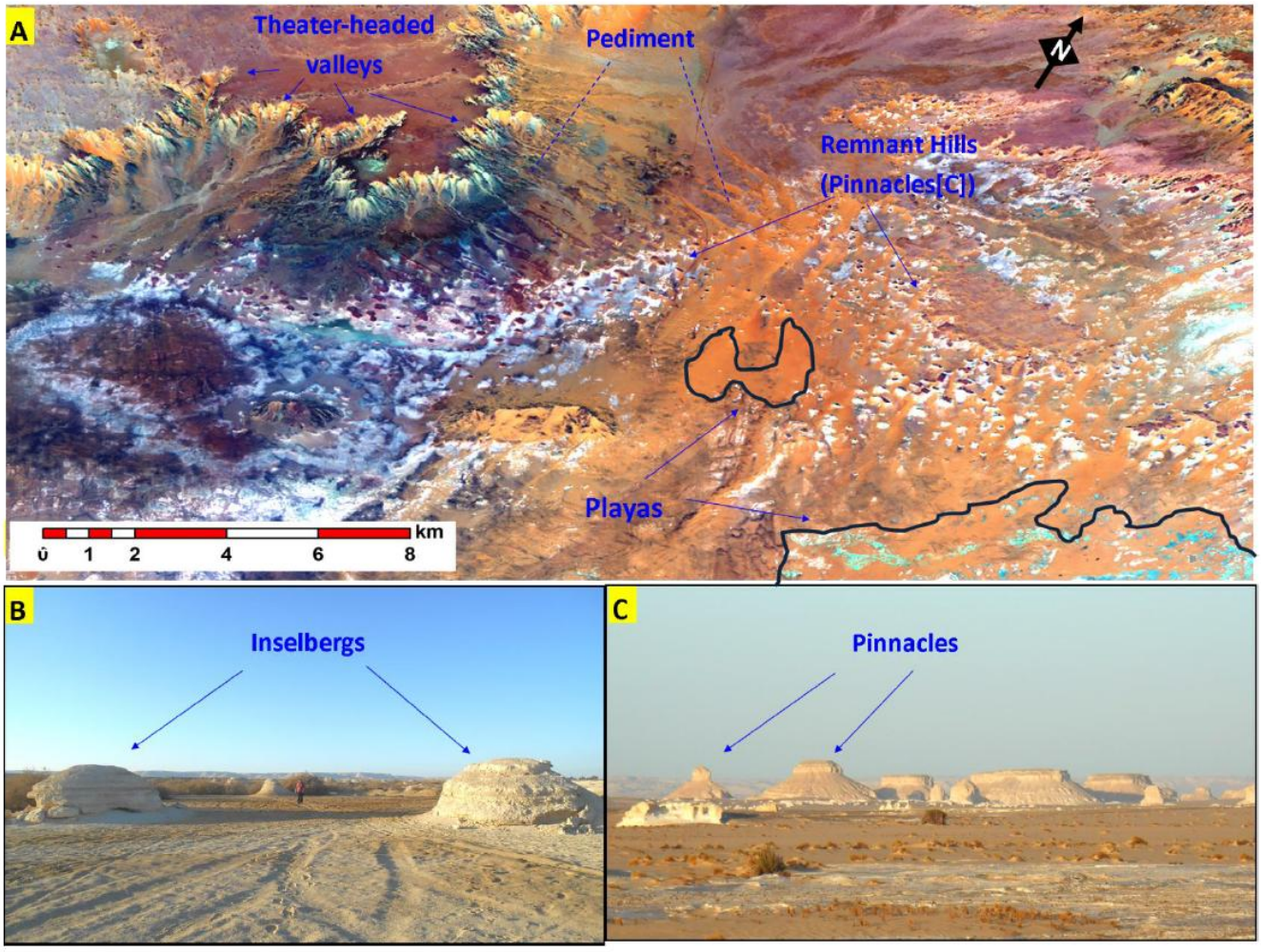

Figure 15

Figure 15

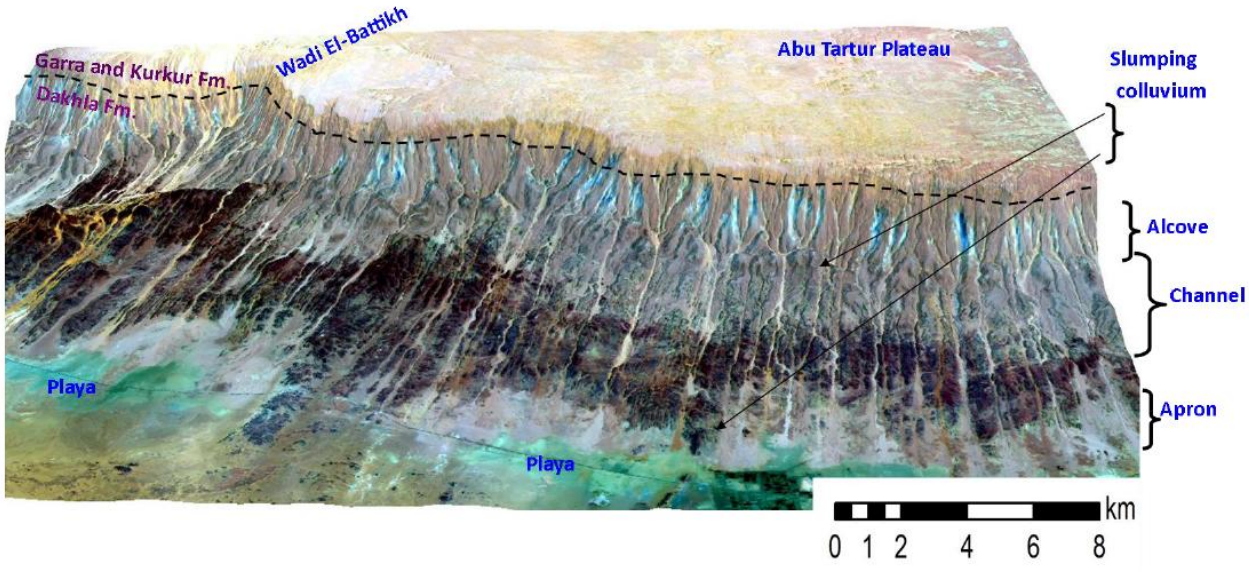

Figure 16

Figure 17

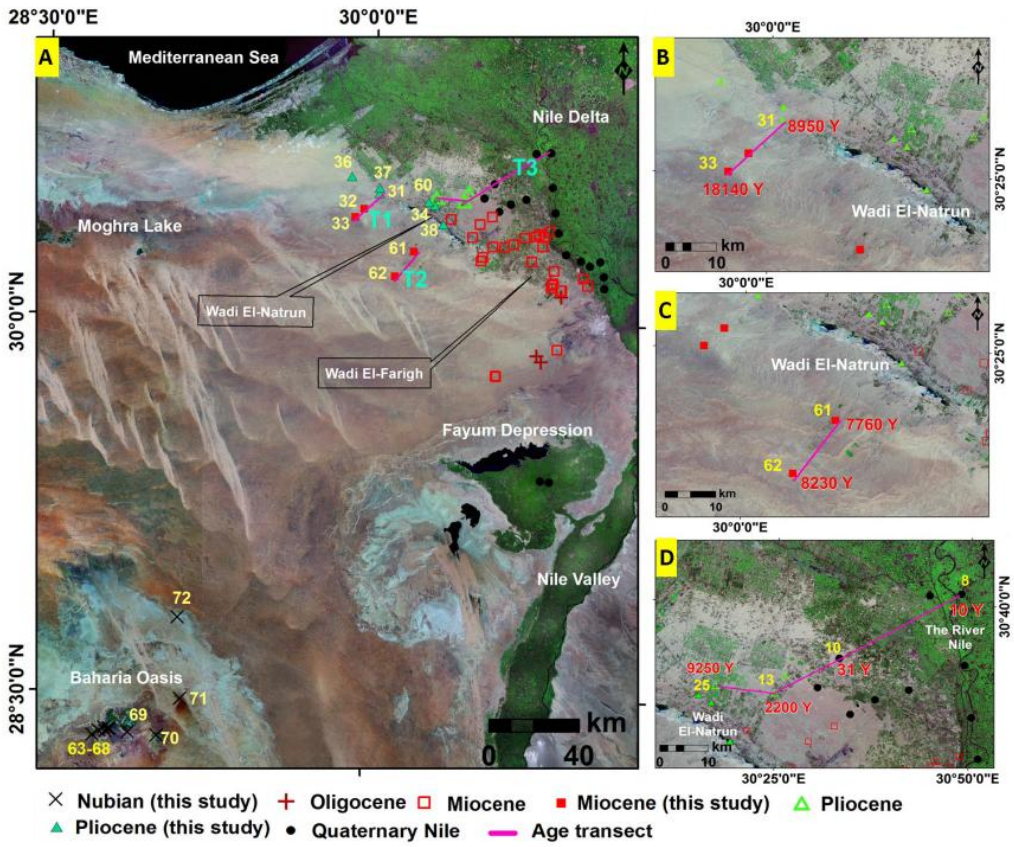

Figure 18

Figure 18

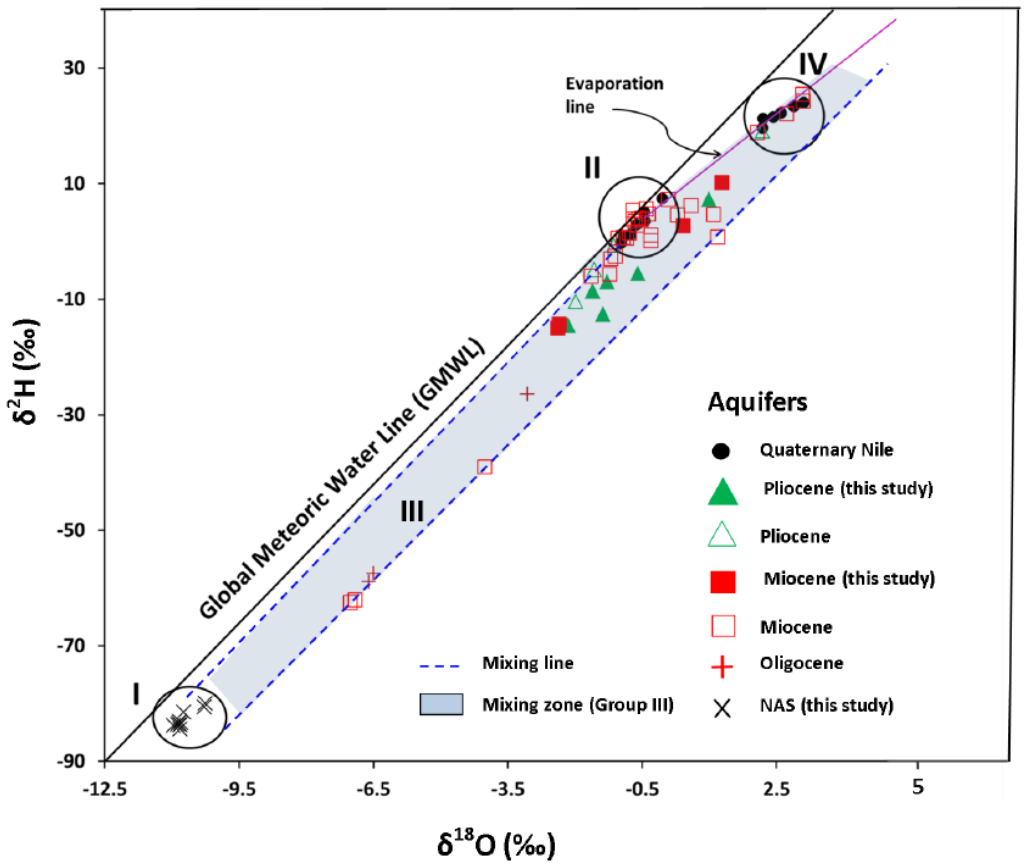

Figure 19

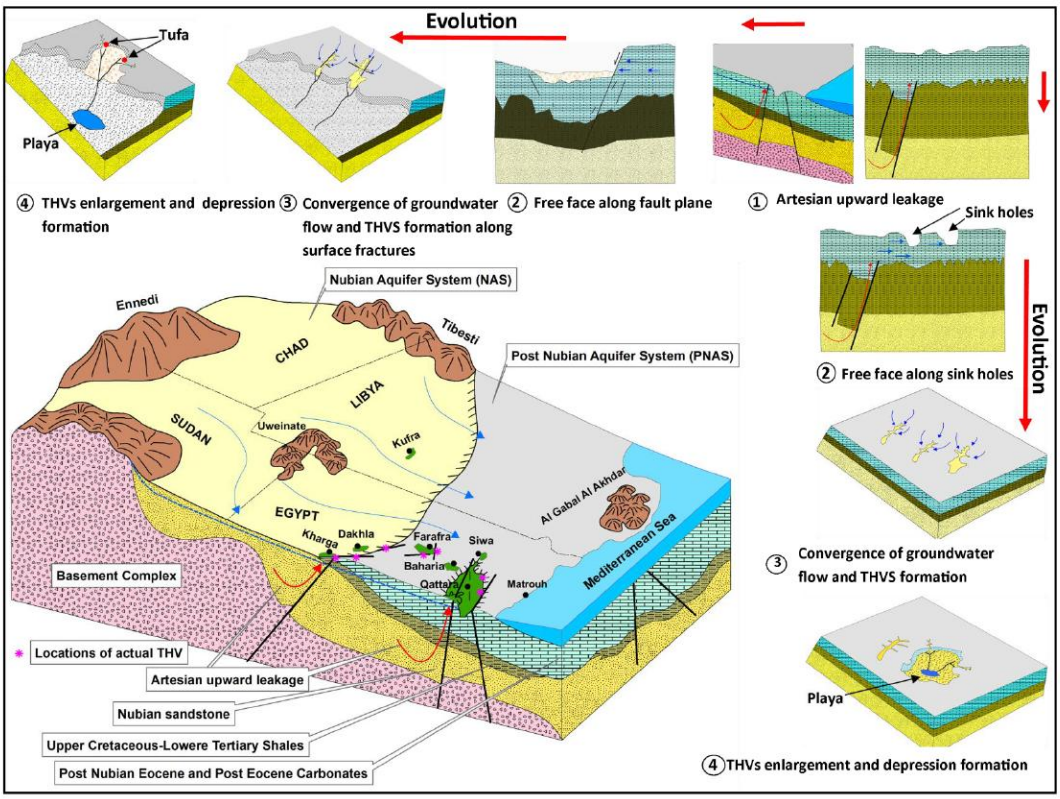

Figure 20

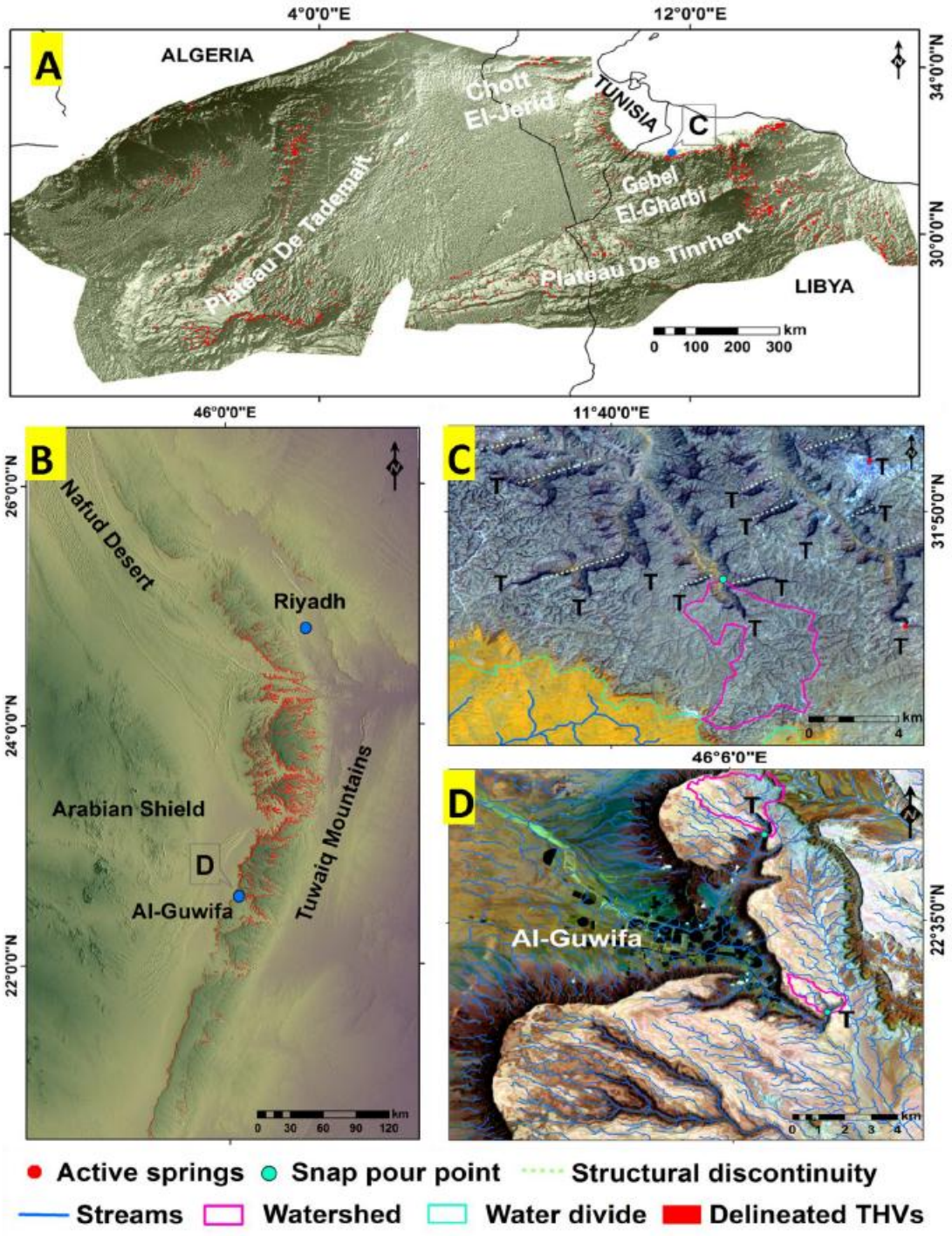

Figure 21